LITHOS 494-495 (2025) 107913

Contents lists available at ScienceDirect

LITHOS

journal homepage: www.elsevier.com/locate/lithos

Sulfur cycling in the gabbroic section of the Oman ophiolite

Ana P. Jesus [a,*], Harald Strauss [b], Mário A. Gonçalves [a,c], Michelle Harris [d], Diogo Silva [c], Martin J. Whitehouse [e], Damon A.H. Teagle [f]

[a] Instituto Dom Luiz, Faculdade de Ciências Universidade Lisboa, Campo Grande C6 piso 1, 1749-016 Lisboa, Portugal
[b] Institute for Geology and Paleontology, University Münster, Correnstr. 24, 48149 Münster, Germany
[c] Departamento de Geologia, Faculdade de Ciências Universidade Lisboa, Campo Grande C6 piso 1, 1749-016 Lisboa, Portugal
[d] School of Geography, Earth and Environmental Sciences, Plymouth University, B526 Portland Square, Drake Circus, Plymouth PL4 8AA, UK
[e] Department of Geosciences, Swedish Museum of Natural History, Box 50 007, SE-104 05 Stockholm, Sweden
[f] School of Ocean and Earth Science, National Oceanography Centre Southampton, University of Southampton, European Way, Southampton SO14 3ZH. UK

ARTICLE INFO

Keywords:
Multiple sulfur isotopes
Oman Ophiolite
Oceanic Crust
Hydrothermal alteration
Sulfide

ABSTRACT

We present sulfur mineralogy and isotope geochemistry from the gabbro transect of the Oman Drilling Project to unravel the sulfur cycle during hydrothermal alteration of the plutonic oceanic crust. The sheeted dike–gabbro transition (Hole GT3A) shows low sulfide-sulfur concentrations ($GT3A_{median}$ = 178 ppm, σ = 4873 ppm) but with great sulfur isotope variability ($\delta^{34}S$ = −12.8 to 14.4 ‰ V-CDT, weighted average + 5.8 ‰) and unusually heavy compositions relative to in-situ or ophiolitic crust. These features are consistent with abiogenic thermochemical sulfate reduction during intense hydrothermal alteration under greenschist facies conditions which formed a low-variance and relatively high-fS_2 assemblage of pyrite ± chalcopyrite ± bornite. The heaviest isotope compositions (+10 to +14 ‰) occur within 10 m of the uppermost gabbro screen suggesting focused fluid-rock exchange with isotope enrichment relative to seawater due to closed-system reservoir effects. The change in isotope compositions from +5 to 0 ‰ in the overlying sheeted dike reflect fluids gradually buffered by magmatic sulfur to signatures similar to the Oman Volcanogenic Massive Sulfide deposits. Hole GT3A represents a deep hydrothermal reaction zone with extensive S and base metal losses and incorporation of up to ~80 % seawater-derived sulfate. The amount of Cu and Zn released in a 1 km^3 crustal section similar to Hole GT3A is ~3 times greater than the average contents of Omani VMS deposits.

The mid to lower crustal section (Holes GT2A and GT1A) mostly preserves MORB sulfur isotope compositions but highly variable sulfide-sulfur contents ($GT2A_{median}$ = 454, σ = 693 ppm, $GT1A_{median}$ = 114, σ = 277 ppm). Away from fault zones, silicate microvein networks enabled variable sulfide and metal remobilization. Magmatic sulfides persist as remobilized remnants along with sulfidation reactions and mild isotopic enrichments (<+2.7 ‰) in secondary sulfides (millerite + siegenite-polydimite$_{ss}$ + pyrite). The mid-lower crustal section experienced redistribution of magmatic sulfur mixed with minor inputs of seawater-derived sulfur (<10 %), under very low fluid/rock ratios and moderate sulfur fugacities, that chiefly preserved base metal abundances in secondary sulfides. The many faulted intervals present in Holes GT1A and GT2A record near complete sulfur and metal leaching of magmatic sulfides without the deposition of secondary sulfides, but preserve sulfate with a Cretaceous seawater sulfate-sulfur isotope signature (+16.1 to +17.3 ‰). These structures are the expression of crustal scale channeled hydrothermal recharge fluid flow and record a previously unaccounted sulfur budget introduced in the deep crust.

1. Introduction

Hydrothermal circulation modifies the composition of the oceanic crust by fixing chemical elements such as magnesium, boron, strontium and sulfur during chemical exchange between seawater and basaltic rock; these reactions take place under progressively higher temperatures with depth leading to mineral transformations up to amphibolite facies temperatures (Alt, 1995). Ultimately, the balance between

* Corresponding author.
E-mail addresses: ana.jesus@fc.ul.pt (A.P. Jesus), hstrauss@uni-muenster.de (H. Strauss), mgoncalves@fc.ul.pt (M.A. Gonçalves), michelle.harris@plymouth.ac.uk (M. Harris), martin.whitehouse@nrm.se (M.J. Whitehouse), damon.teagle@southampton.ac.uk (D.A.H. Teagle).

https://doi.org/10.1016/j.lithos.2024.107913
Received 26 March 2024; Received in revised form 6 December 2024; Accepted 8 December 2024
Available online 13 December 2024

hydrothermal alteration, submarine volcanic emissions and riverine inputs regulates the composition of the ocean through time and can modify the mantle through the subduction of altered oceanic crust (Plank and Manning, 2019). Sulfur is a crucial element for tracing global biogeochemical and planetary cycles: the mass exchanges and isotopic fractionations of sulfur enable identifying the chemical pathways and quantify elemental fluxes between surface and endogenous reservoirs within a wide range of temperatures and redox conditions (Canfield, 2004). Sulfur cycling in the oceanic crust has been studied on drill core samples obtained through scientific ocean drilling and in ancient oceanic crust exposed on land in ophiolites. Drilling in the thick crust of fast spreading ridges has intersected the volcanic rocks and the sheeted dikes (Alt et al., 1989; Alt et al., 1995). However, after more than five decades of ocean drilling, Ocean Drilling Program Hole 1256D remains the only borehole to reach the sheeted dike-gabbro transition, intersecting the "high level" or "isotropic" gabbros of the axial melt lens (Teagle et al., 2010; Wilson et al., 2006). Submersible dives into lower crust exposed by rifting has enabled mapping and sampling of deep cumulate gabbros formed on the fast spreading East Pacific Rise (EPR) at Hess Deep (Gillis, 1995; Gillis et al., 2001) and Pito Deep (Barker et al., 2010; Heft et al., 2008) but intact sections remain un-sampled leading to poor knowledge of magmatic accretion processes and the associated hydrothermal exchanges (Kelemen et al., 1997; Lecuyer and Reynard, 1996; McCollom and Shock, 1998).

Due to these constraints, there is little knowledge of sulfur behavior in deep plutonic rocks formed at fast spreading ocean ridges. Evidence shows that the permeable volcanic section of the oceanic crust experiences low temperature (<100 °C), oxidative alteration that leads to sulfur loss and mild isotopic enrichments ($\delta^{34}S \sim +1.6$ ‰; ODP Hole 504B, Alt et al., 1989) relative to a canonical MORB mantle value of $+0.1 \pm 0.3$ ‰ (Sakai et al., 1984). H_2 produced during iron oxidation can support chemoautotrophs (Bach and Edwards, 2003) producing large fractionations down to a $\delta^{34}S$ value of −26.1 ‰ in the volcanic section (Troodos; Alt, 1994) resulting from microbial sulfate reduction (MSR) under open system conditions. Mixing of upwelling hydrothermal fluids with cold seawater can form sulfide mineralization at the lava-dike transition (Alt et al., 2010), with $\delta^{34}S$ values up to +3 ‰ (Alt et al., 1989). During active axial hydrothermal circulation, increasing temperatures from greenschist (>250 °C) to lower amphibolitic facies conditions (>350 °C) in the sheeted dikes and the underlying dike-gabbro transition precludes biologically mediated processes and incorporation of seawater derived sulfur occurs via thermochemical sulfate reduction (TSR) pathways (Shanks, 2001).

Sulfur isotopic enrichments documented in the intrusive upper crustal section are significantly higher in ophiolites (<+10 ‰; Alt, 1994) compared to those observed in modern crust (<+3.1 ‰, Alt et al., 1989; Alt et al., 1995; Barker et al., 2010). Furthermore, the dike–gabbro transition is thought to represent the reaction zone where metals for the genesis of Volcanogenic Massive Sulfide (VMS) deposits are sourced (Alt, 1995; Hannington, 2014). Epidosites, mineral associations of granoblastic epidote-quartz-titanite, have long been considered to represent the depleted endmembers of sulfur and metal leaching at the deep reaction zone. Despite clear evidence for metal mobilization in in-situ oceanic crust (Alt et al., 1996; Alt et al., 2010; Gillis, 1995; Gillis et al., 2001; Heft et al., 2008; Patten et al., 2016), epidosites have only been documented in ophiolites (Harper et al., 1988; Harris et al., 2015; Jowitt et al., 2012; Nehlig et al., 1994; Richardson et al., 1987). Recent work in the Oman ophiolite has challenged the view that epidosites are restricted to the deep reaction zone (Gilgen et al., 2016) and proposed that they are formed by late, oxidized, Fe-poor fluids, unlikely to form VMS deposits (Richter and Diamond, 2022).

Differences between in-situ oceanic and ophiolitic lower crustal sections are seemingly less pronounced. However, sampling deep crustal sections of in-situ oceanic crust is restricted to tectonically exposed sections, most common on slow-spreading ridges. Uplifted sections of lower crust that are directedly exposed to seawater can display oxidative, lower temperature alteration enabling MSR processes (Alford et al., 2011). Otherwise, sulfur isotopic enrichments decrease throughout the gabbroic lower crust towards values below +2.5 ‰ although sections affected by channeled fluid flow may record heavier isotopic compositions (ca. +6 ‰ Alt, 1994; Puchelt et al., 1996; Delacour et al., 2008a; Delacour et al., 2008b).

The Samail Ophiolite in the Sultanate of Oman (**Fig. 1**B) provides a unique sample of the oceanic crust and upper mantle exposed on land that has been extensively studied since the late 1970's. The International Continental Scientific Drilling Program (ICDP) Oman Drilling Project (OmanDP; Kelemen et al., 2020) enabled unprecedented, continuous sampling of critical sections of the ophiolite crust and mantle through drilling of a number of short (≤400 m) diamond coring drill holes from representative sections of the mid- to lower plutonic crust of the Samail ophiolite (**Fig. 1** A). Sulfide minerals are easily modified by oxidation and weathering processes under surface conditions, therefore OmanDP samples provide an exceptional opportunity to investigate sulfur and metal cycling in pristine rocks from the oceanic crust. A profile in the Samail Ophiolite based on surface samples by Oeser et al. (2012) showed elevated $\delta^{34}S$ values (up to +5 ‰) and low sulfide S-contents in the dike-gabbro transition that were attributed to TSR followed by oxidation and leaching; the lower crust and mantle section preserved near-MORB $\delta^{34}S$ values and non-zero, mildly negative $\Delta^{33}S$ values (down to −0.042 ‰). Building on Oeser et al. (2012) findings, we present detailed sulfide mineralogy and results from whole-rock sulfur isotope geochemistry complemented with data from in-situ techniques covering a representative profile of the intrusive oceanic crust including: 1) the upper crustal sheeted dike complex and the transition to the high level gabbros (Hole GT3A); 2) the mid-crustal section at the transition from foliated to layered gabbros (Hole GT2A) and; 3) a sequence of lower crustal layered gabbros (Hole GT1A) about 1000 m stratigraphically above the crust-mantle transition zone. To understand the pathways and isotopic fractionation mechanisms of sulfur from magmatic conditions throughout the various stages of oceanic hydrothermal alteration, our sampling covers a spectrum from fresh rocks to those recording moderate to complete hydrothermal recrystallisation, including highly deformed rocks from deep oceanic fault-zones crosscutting the layered gabbros (Zihlmann et al., 2018). Finally, to assess the metal mobility and elucidate on the potential source rocks for VMS deposits, we make use of comprehensive whole-rock profiles obtained during core logging by the OmanDP science team (Kelemen et al., 2020).

2. Geological setting

The Samail ophiolite is the largest and best preserved slice of ancient ocean lithosphere on land (Nicolas et al. (2000) and references therein). Here we highlight the current views on the oceanic crust accretion and hydrothermal alteration, followed by an overview of the main features for the 3 drillholes based on the multidisciplinary core logging carried out by the OmanDP phase 1 scientific party (Kelemen et al., 2020).

2.1. The Samail Ophiolite and current views on the oceanic crust accretion and alteration

The Samail Ophiolite represents an exceptionally large fragment of the Tethyan ocean lithosphere with ca 500 km long, 200 km width and 2–20 km thickness that was preserved from post-obduction tectono-metamorphic events (Nicolas et al., 2000). Its classic Penrose stratigraphy (Anonymous, 1972) became the template for the structure of the oceanic crust in fast-spreading ridges such as the EPR (Pallister and Hopson, 1981). The ophiolite records a polygenetic history (Alabaster et al., 1982) starting with a main axial stage of crustal accretion, during which the Penrose-like crustal architecture was developed, and the voluminous V1-Geotimes axial lavas erupted. A second magmatic stage comprises incompatible element depleted, low-Ti off-axis volcanism (V2 lavas) and late intrusives (gabbronorites, wehrlites; Benoit et al., 1996;

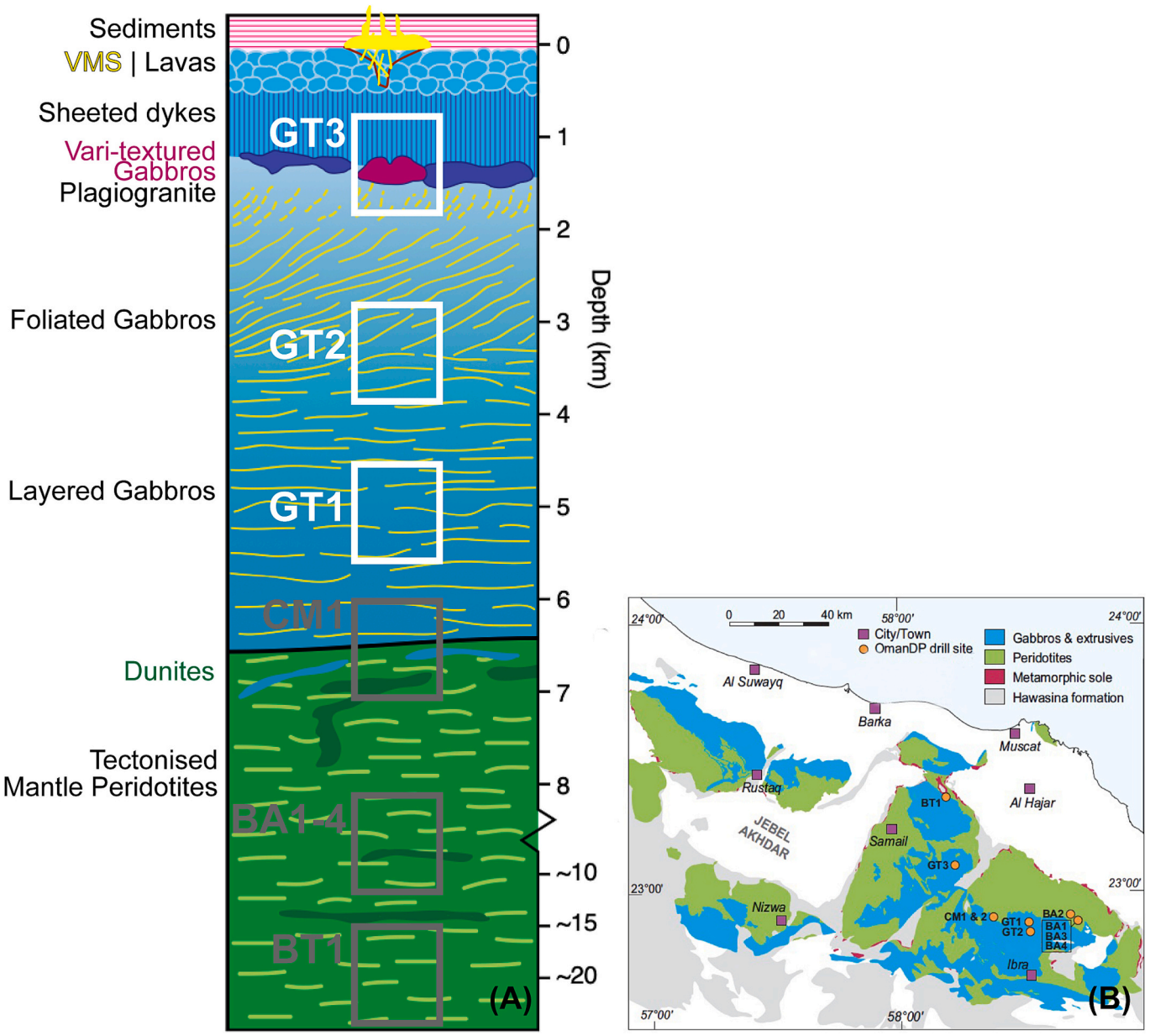

Fig. 1. **(A)** idealized stratigraphic column for the Samail Ophiolite (adapted from Kelemen et al., 2020) showing the approximate stratigraphic depths of the sections studied. **(B)** Location of the Holes GT1A (22°53.535′N, 58°30.904′E, layered gabbros) and GT2A (22°51.793′N, 58°31.191′E; foliated-layered gabbros) and gabbro-dike transition Hole GT3A (23°06.845′N, 58°12.703′E) in relation to the regional geology.

Koepke et al., 2009), consistent with hydrous melting of a progressively depleted mantle source. This evolution has led to considerable debate about whether the Samail ophiolite was formed at a typical Mid-Ocean Ridge (MOR) or in a subduction initiation setting (Belgrano et al., 2019; Godard et al., 2006; Lippard, 1986). Zircon U/Pb dating place axial magmatism at 96 Ma whereas post-ridge magmatic activity extended until 95 Ma (Rioux et al., 2021).

Current views on the oceanic crust are based on seminal geological and geophysical observations on the seafloor and ophiolites (Alt, 1995). They propose that fast-spreading ridges comprise an upper crust with ca. 3 km where lavas grade into the sheeted dike complex via a ~ 100 to 300 m-thick transition zone where subvertical dikes are increasingly common. The dike complex roots into a thin axial melt lens (AML; MacLeod and Yaouancq, 2000; Gillis, 2008) the level of which can vary dynamically through time due to eruption/replenishment cycles (Coogan et al., 2003). The AML is overlain by a thermal boundary layer that separates the vigorous hydrothermal convective system responsible for the generation of seafloor hydrothermalism and SMS/VMS deposits (France et al., 2021; Wilson et al., 2006) from the underlying deeper hydrothermal system affecting the lower crust.

Much of the lower crust beneath the ridge is in a mushy state, down to the Moho Transition Zone (MTZ). The exact mechanism of crustal accretion continues to be debated (e.g., Coogan et al., 2006; Zhang et al., 2021) and is strongly dependent on the mechanisms for cooling of the crust and the geometry of hydrothermal circulation. Potential processes for heat removal of the lower crust include a millimeter-scale inter- and transgranular vein networks infilled with amphibole (Bosch et al., 2004; Manning et al., 2000). Because these may not be sufficient to extract heat from depth, large scale corridors of focused fluid flow extending from the base of the sheeted dike down to the MTZ under greenschist facies (~300 °C) up to very high temperature conditions (~880 °C) have also been proposed, (Coogan et al., 2006; Zihlmann et al., 2018). Noticeable examples of such corridors in Oman are the Al Asih (Abily et al., 2011) and Zihlmann-Müller- fault zone-ZMFZ (Zihlmann et al.,

2018) where cooling was largely facilitated by introduction of seawater-derived hydrothermal fluids to great large depths in the crust resulting in the cooling from magmatic conditions to greenschist facies temperatures.

2.2. Main features of drillholes OmanDP Holes GT1A, GT2A, GT3A

The three OmanDP drillholes investigated were diamond-cored to ~400 m and petrographically and instrumentally described to better than scientific ocean drilling standards (Kelemen et al., 2020) (Fig. 2). The lower crustal (GT1A) and mid-crustal sites (GT2A) are located in Wadi Gideah (Tayin Massif) and estimated to lie ~1400 m and ~ 3300 m above the (crust-)Mantle Transition Zone (MTZ), respectively (**Fig. 1**, Fig. 2). The gabbro-dike transition site (GT3A) is located in Wadi Aswad in the Samail Massif, approximately 40 km west of Wadi Gideah and is estimated to be collared ~4100 m above the MTZ. All drill sites are located in domains without the influence of the second (V2) magmatic stage magmatism and their magmatic features document the V1 crustal accretion stage of the Samail paleoridge (Goodenough et al., 2014). All drilling depths refer to the *Chikyu Curated Depth* (CCD) scale (Kelemen et al. (2020).

2.2.1. Lithostratigraphy

Olivine gabbro is the most abundant rock type in both Holes GT1A and GT2A (65.9; 65.4 % respectively) followed by olivine-bearing gabbro (21.5 %;15.8 %) with subordinate intercalations of other rock types (Fig. 2). Magmatic units in Holes GT1A and GT2A were defined based on modal, grain-size and layering intensities downhole. Grain-size is most commonly fine to medium with rare pegmatitic layers, that are more common in Hole GT1A. Some fine-grained gabbros in Hole GT2A are porphyritic with large, zoned, plagioclase phenocrysts. Layering and foliation are present in both holes, but dip more steeply in Hole GT2A than in Hole GT1A, where layers have gentle dips sub-parallel to the paleo-Moho. There is no clear boundary between foliated and layered gabbros, and both rock types occur throughout Hole GT2A.

Hole GT3A sampled the dike-gabbro transition, and is subdivided into four major magmatic units (Fig. 2) including an Upper and Lower Sheeted Dike sequence with more than 95 % steeply dipping dikes with mean thickness estimated to be 0.58 m comprising (porphyritic) diabase with chilled, basaltic to glassy margins. These dikes are separated by two gabbro sequences which nonetheless include significant amounts of dikes (~46.5 %) but have distinctive petrography. The thin Upper Gabbro (111.02 to 127.89 m downhole) is dominantly olivine (bearing) gabbro whereas oxide (disseminated) gabbro prevails in the Lower Gabbro (from 233.84 m). Swarms of dikelets and magmatic breccias of tonalite and diorite occur at the transition from the Lower Dikes to the Upper Gabbro sequence, wherein oxide gabbros grade upward to leucodiorite. Dike-gabbro crosscutting relationships suggest that the Upper Gabbro represents a younger paleolevel of the AML relative to the highly differentiated oxide gabbros of the Lower Gabbro Sequence (Engelhardt et al., 2022; France et al., 2021; Kelemen et al., 2020). Unlike ODP Hole 1256D (Alt et al., 2010; Wilson et al., 2006) no continuous region of granoblastic hornfels resulting from contact metamorphism of the dikes was present in Hole GT3A although granoblastic patches have been reported in the surrounding outcrops (France et al., 2021). Microgranular domains with granoblastic textures representing stopped blocks of hydrothermally altered and metamorphosed dikes are present at ~243 m (Engelhardt et al., 2022) and 323–326 m depths in Hole GT3A (Kelemen et al., 2020) (Fig. 2).

2.2.2. Alteration and deformation

Total alteration, defined as the weighted average of background alteration plus patches, vein halos and deformation-related alteration, is higher in Holes GT1A (60 %) and GT3A (54 %) than in Hole GT2 A (44 %). All sections record early alteration under amphibolite facies conditions (brown amphibole), progressing through greenschist (green amphibole + chlorite + albite + epidote) and late sub-greenschist facies (zeolites+prehnite+calcite) (Kelemen et al., 2020).

Brown amphibole blebs replace clinopyroxene in Holes GT1A and 2 A and are less common in Hole GT3A (Engelhardt et al., 2022), where

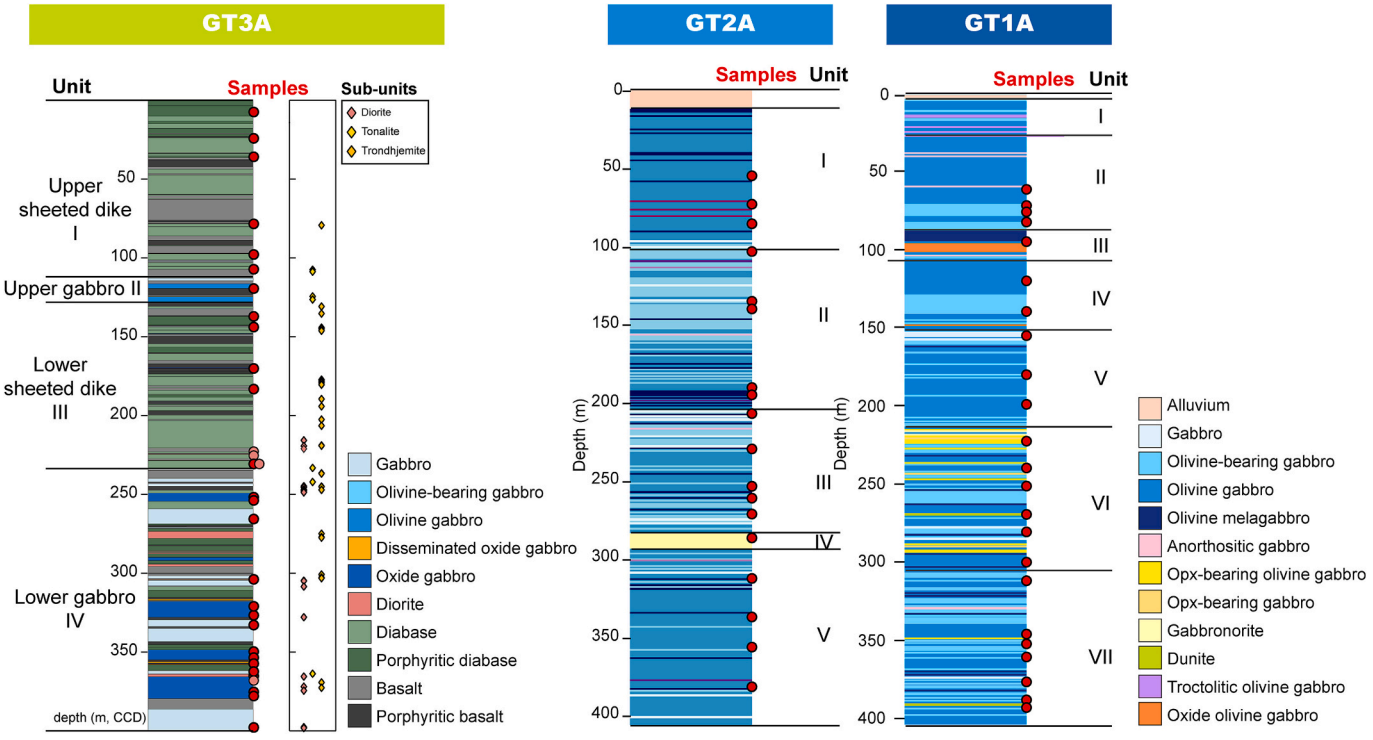

Fig. 2. Lithological columns for OmanDP Holes GT1A, GT2A and GT3A (adapted from Kelemen et al., 2020). All depth scales in m CCD (*Chikyu Curated Depth* as in Kelemen et al. (2020).

fibrous green amphibole is the most common mineral pseudomorphically replacing clinopyroxene. Olivine is replaced by chlorite + oxides (rarely serpentine) although in Hole GT2A, talc or brown phyllosilicates are also common. Rare olivine phenocrysts in the Hole GT3A diabase or in the matrix of olivine gabbros are completely replaced by mixtures of smectite-chlorite + actinolite + opaques. Epidote (s.l.) is significantly more common in Hole GT3A, where it extensively replaces igneous plagioclase in several intervals; plagioclase is also extensively replaced by albite or zeolites (thompsonite; also present in Holes GT1A and GT2A). In the lower/mid-crustal sections (GT1A-GT2A), plagioclase is more commonly replaced by chlorite, whereas albitization prevails in intensely altered intervals with loss of primary texture. Most Hole GT2A rocks feature an intergranular chlorite vein network that replaces plagioclase along the margins of microcracks. Downhole variations are conspicuous for few alteration minerals: i) calcite and oxy-hydroxides are more common in the uppermost part of each hole and; ii) Hole GT3A features a clear downhole increase in epidote±prehnite (Kelemen et al., 2020).

Vein mineral fill and associated halos follows the relative order of formation outlined above. Vein densities increase towards fault zones and deformation-related alteration is most commonly associated with lower temperature, sub-greenschist mineral paragenesis (~270–100 °C). Additionally, Holes GT1A and GT2A have wide (2–10 m) intervals of fault rock with associated anhydrite veins (Kelemen et al., 2020; Teagle et al., 2019).

Pre-drilling site survey geological mapping identified a 251/55°SE structure (Zihlmann et al., 2018) ca. 300 m north-east of Site GT1 named Zihlmann-Müller Fault Zone (ZMFZ; Kelemen et al., 2020). This normal fault zone with convincing *syn*-oceanic origin comprises ~1 m fault-gauge and a > 4 m alteration halo ranging from greenschist (chlorite-epidote) to zeolite facies (carbonate-zeolite) conditions with formation of pyrite ± chalcopyrite. Copper slags from ancient ore processing are common in the vicinity. The ZMFZ was projected to be intersected by Hole GT1A between 145 and 310 m depth and is likely one of the main fault structures identified at ca. 200 m. However, unexpectedly Hole GT1A intersected 7 major faut zones and 14 minor structures with associated intense deformation, alteration and veining, so the exact correlation to the ZMFZ is not possible. Hole GT2A includes 20 main fault-zones and a total > 250 m of moderate to complete brittle deformation, more evenly distributed than in Hole GT1A (see. Fig. 5B, ahead). In Hole GT3A deformation is most commonly concentrated along dike margins and postdates vein formation or is contemporaneous with the latest zeolite vein generation. The intervals with most significant brittle deformation and veining are between 160 and 200 m and 360–400 m (Fig. 2).

3. Methods

3.1. Sampling strategy and sample preparation

Sampling took place aboard R/V *Chikyu* during ChikyuOman2017 Phase 1 core logging activities (Kelemen et al., 2020). Most samples were quarter cores with lengths between 5 cm (for HQ = 63.5 mm diameter) and 10 cm (for NQ = 47.6 mm diameter). 73 samples were selected for mineralogical study and S isotopic characterization distributed amongst Holes GT1A, GT2A and GT3A, with care taken to avoid the uppermost weathered intervals and focusing on intervals with visible sulfide (Table 1). Sample referencing follows the original on-site labelling during core handling and curation (Kelemen et al., 2020).

Following macroscopic description, thin section billets were made from representative portions of the sample and the remainder core powdered at the Geology Department Faculdade Ciências Lisboa/IDL, for whole-rock sulfur geochemical analysis. Samples were split with diamond saws and all surfaces abraded in emery wheels to remove any metal contaminants. Whole-rock powders for sulfur elemental and isotopic analysis were obtained by coarse crushing in a hardened steel roll crusher and final pulverization in an agate mill.

3.2. Petrography and mineralogy

Due to microscopic scale variations in alteration and sulfide distribution, the samples processed for sulfur isotopic geochemistry were studied in detail. Petrographic analysis of polished thin sections took place under transmitted and reflected light, enabling visual estimates of: 1) total alteration % by weighted average of each magmatic mineral species; 2) modes for remobilized, magmatic and hydrothermal sulfide, as reported in section 4.1. Total alteration % does not include veins and can thus be considered as a minimum estimate for each thin section. Total sulfide modes were determined by image analysis using Leica Software by averaging 3 random areas. All data are available in Supplementary Material 1 (SM 1, Table 1).

3.3. Electron probe micro-analysis

Petrographic observations reported in this work were validated via Electron Microprobe analysis of silicate (unpublished results) and sulfide mineral assemblages Supplementary Material SM1 (Table 2). Mineral major element compositions were determined on polished sections, covered in a 20 nm-thick carbon coating at the Geology Department Faculdade Ciências Lisboa/IDL using a JEOL-JXA 8200 electron probe microanalyzer (EPMA) equipped with four wavelength-dispersive spectrometers (WDS), six analyzer crystals (LIF, LIFH, PET, PETH, TAP and LDED2), secondary and back-scattered electron detectors, and an energy-dispersive spectrometer (EDS). Measurements were made with a 20s acquisition time for the peaks, and 5 s for the background. The accelerating voltage was 15 keV, with a beam current of 25 nA and a beam diameter of 5 μm. Natural mineral and metallic standards from Astimex Scientific Ltd. were used.

3.4. Sulfur isotopes- whole rock

Sulfur extraction, measurements and isotope analyses were performed at the Institut für Geologie und Paläontologie, University of Münster. Total sulfur concentrations (TS_{Meas}) were measured using an Eltra CS-580 sulfur/carbon analyzer with a detection limit of 0.01 wt% and an estimated analytical uncertainty of 3 % relative. 10–20 mg of whole-rock powder was combusted at 1350 °C in a porcelain crucible under an O_2-atmosphere. These data were used to determine the amount of sample for the sequential sulfur extractions and to assess if the extractions were complete. All sulfur concentrations in the text refer to those obtained by gravimetry, as described below.

Sulfur extraction for subsequent isotope analyses was performed by a sequential wet chemical procedure. Acid Volatile Sulfides (AVS, including monosulfide phases such as pyrrhotite or sphalerite) and Cr-reducible Sulfur (CRS, including disulfides such as pyrite, chalcopyrite or bornite), were extracted in closed glass digestion vessels under a N_2-atmosphere using 6 M HCl and 1 M $CrCl_2$-HCl, respectively (Canfield et al., 1986; Rice et al., 1993). Released H_2S was firstly precipitated as ZnS in a 3 % acetic zinc acetate solution and then as silver sulfide (Ag_2S) using a 0.1 M $AgNO_3$ solution. The sample residue following the AVS-CRS extraction ($TS_{sulfide}$=AVS + CRS) was filtered and acid-soluble sulfate (TS_{SO4}) was precipitated as $BaSO_4$ using an 8.5 % $BaCl_2$ solution. The mass of each sulfur species was determined via gravimetry, their sum representing the total sulfur extracted: $TS_{Ext} = TS_{sulfide}$(AVS + CRS) + TS_{SO4}. Comparison of total sulfur extracted wet-chemically (TS_{Ext}) with that measured using the sulfur/carbon analyzer provides excellent agreement ($r = 0.99$) with deviations mostly for samples with low S concentration (S < 500 ppm) that approach the lower detection limit of the Eltra furnace (SM2, Fig. 1).

$\delta^{34}S$ was determined for all three sulfur species using a a Thermo-Scientific Delta V Advantage mass spectrometer coupled with a Flash EA IsoLink elemental analyzer. Between 0.290 and 0.440 mg of sample

Table 1
Sulfur and sulfate contents and corresponding $\delta^{34}S$ isotope composition extracted from bulk rocks.

		AVS			CRS			Sulfates			Sulfide-S (ppm)	TS Ext (ppm)	SO_4/TS	$\delta^{34}S$ Bulk Sulfide
Ref	Lithology	S (ppm)	$\delta^{34}S$ (‰)	± (‰)	S (ppm)	$\delta^{34}S$ (‰)	±	S (ppm)	$\delta^{34}S$ (‰)	±(‰)				
GT3A-9Z1 7.0–12.0	Diabase				6	−0.5					6	6		-0.5
GT3A-22Z2 4.0–9.0 DIA	Diabase				2	0.5		3			2	4	0.64	0.5
GT3A-26Z3 10.0–15.0	Diabase				60	5.1	0.001	29			60	89	0.32	5.1
GT3A-41Z3 22.0–27.0	Basalt				212	−12.8	0.003				212	212		−12.8
GT3A-48Z1 11.0–13.0	Basalt				862	13.2	0.018				862	862		13.2
GT3A-52Z1 35.0–40.0	Basalt				1060	11.3	0.001	25			1060	1084	0.02	11.3
GT3A-56Z1 59.0–64.0	Ol Gabbro				650	13.3	0.002	15			650	665	0.02	13.3
GT3A-63Z1 0.0–6.0	Plag-cpx phyric Basalt				462	13.6	0.017				462	462		13.6
GT3A-65Z1 36.0–39.0	Basalt				97	8.8	0.021	8			97	105	0.07	8.8
GT3A-73Z4 9.0–14.0 GB	Oxide Gabbro				4	3.2	0.035	3			4	7	0.44	3.2
GT3A-78Z1 36.0–41.0	Basalt				94	7.1	0.009	3			94	98	0.03	7.1
GT3A-91Z4 80.0–85.0	Basalt (Dior Xen)				105	9.4	0.056	20			105	125	0.16	9.4
GT3A-94Z1 27.0–32.0 BAS	(Basalt / Diorite) Basalt fraction				4032	10.4	0.041				4032	4032		10.4
GT3A-94Z1 27.0–32.0 DIOR	(Basalt / Diorite) Diorite fraction				36	3.8	0.009				36	36		3.8
GT3A-100Z4 67.0–72.0	Oxide Gabbro				21	5.4	0.052	2			21	23	0.09	5.4
GT3A-101Z3 66.0–71.0	Basalt				1545	11.7	0.008				1545	1545		11.7
GT3A-109Z1 27.0–35.0	Gabbro				37	8.4	0.012	14			37	51	0.27	8.4
GT3A-121Z4 7.0–15.0	Oxide Dissiminated Gabro				43	8.6	0.027				43	43		8.6
GT3A-128Z2 62.0–70.0	Oxide Gabbro				714	5.1	0.008				714	714		5.1
GT3A-130Z1 55.0–63.0 GB	Oxide Gabbro				837	10.2	0.020				837	837		10.2
GT3A-132Z2 54.0–62.0	Gabbro				8	3.6	0.023	1			8	10	0.14	3.6
GT3A-137Z4 26.0–34.0	Oxide Gabbro				103	5.9	0.007				103	103		5.9
GT3A-139Z1 5.0–13.0	Oxide Gabbro				1452	5.2	0.010	19			1452	1472	0.01	5.2
GT3A-140Z2 22.0–30.0	Plag-cpx phyric Basalt				238	5.0	0.059	3			238	241	0.01	5.0
GT3A-141Z4 43–51	Pyrite Epidote patch				24,902	8.6	0.013				24,902	24,902		8.6
GT3A-142Z4 61.0–69.0 DIOR	Diorite				1575	7.1	0.023	35			1575	1610	0.02	7.1
GT3A-143Z4 24.0–32.0	Oxide Gabbro				64	4.0	0.037				64	64		4.0
GT3A-146Z1 57.0–65.0	Oxide Gabbro				11,334	6.1	0.138	76	4.9		11,334	11,410	0.01	6.1
GT3A-146Z4 17.0–21.0	Oxide Gabbro				144	6.3	0.031	37			144	180	0.20	6.3
GT3A-155Z3 21.0–29.0	Oxide Gabbro				428	0.8	0.033	12			428	440	0.03	0.8
GT2A-24Z2 31.0–36.0	Ol gabbro				149	1.4	0.039	5			149	153	0.03	1.4
GT2A-31Z1 70.0–75.1	Ol gabbro				151	1.5	0.077	0.4			151	152	0.00	1.5
GT2A-36Z1 50.5–55.5	Ol gabbro				483	1.1	0.014	20			483	503	0.04	1.1
GT2A-45Z1 35.0–40.0	Ol gabbro				522	1.0	0.081	11			522	533	0.02	1.0

(*continued on next page*)

Table 1 (*continued*)

Ref	Lithology	AVS			CRS			Sulfates			Sulfide-S (ppm)	TS Ext (ppm)	SO_4/TS	$\delta^{34}S$ Bulk Sulfide
		S (ppm)	$\delta^{34}S$ (‰)	± (‰)	S (ppm)	$\delta^{34}S$ (‰)	±	S (ppm)	$\delta^{34}S$ (‰)	±(‰)				
GT2A-55Z2 65.0–70.0	Ol gabbro				135	1.2	0.063	4			135	139	0.03	1.2
GT2A-58Z1 15.0–20.0	Ol bearing Gabbro				119	1.9	0.025	18			119	137	0.13	1.9
GT2A-67Z3 58.0–68.0	Ol gabbro				2951	1.8	0.018	11			2951	2962	0.00	1.8
GT2A-76Z3 61.0–68.0	Troctolite	0.1			65	2.1	0.107	5			65	70	0.07	2.1
GT2A-78Z1 73.0–81.0	Ol gabbro				2			111			2	113	0.99	
GT2A-83Z1 74.5–82.0	Ol-bearing Gabbro	230			228	1.0	0.025	7			458	465	0.01	0.5
GT2A-92Z4 11.0–20.0	Ol gabbro				450	1.0	0.037	77			450	527	0.15	1.0
GT2A-100Z4 14.0–21.0	Ol gabbro				1233	1.3	0.020	42			1233	1275	0.03	1.3
GT2A-100Z4 44.0–50.0	Ol gabbro				54	−0.7		197	17.3	0.01	54	251	0.78	−0.7
GT2A-104Z4 31.0–39.0	Ol gabbro				288	0.8	0.034	2			288	291	0.01	0.8
GT2A-108Z1 34.0–44.0	Ol-bearing Gabbronorite				614	2.1	0.014	0.2			614	614	0.00	2.1
GT2A-115Z1 40.0–50.0	Ol gabbro				563	1.4	0.032				563	563		1.4
GT2A-123Z3 54.0–60.0	Ol gabbro				705	1.2	0.007	36			705	741	0.05	1.2
GT2A-133Z3 26.0–33.0	Ol gabbro				729	0.6	0.079	27	5.7		729	756	0.04	0.6
GT2A-139Z4 82.0–89.0	Ol gabbro				1566	0.7	0.000				1566	1566		0.7
GT2A-149Z2 17.0–25.0	Ol gabbro				57			24			57	82	0.30	
GT1A-25Z3 5.0–10.0	Ol Gabbro	28	1.9	0.04	283	1.0	0.096	24	2.8		310	334	0.07	1.1
GT1A-30Z1 55.0–60.0	Ol Gabbro	3	1.8		48	1.8		5			52	57	0.09	1.8
GT1A-31Z2 20.0–25.0	Ol bearing Gabbro	337	0.3	0.04	712	0.9	0.005	109	3.3		1050	1159	0.09	0.7
GT1A-33Z3 45.0–50.0	Ol Gabbro				499	1.6	0.006				499	499		1.6
GT1A-39Z1 3.0–12.0	Ol Melagabbro	25	1.4		172	1.2	0.012	13			197	211	0.06	1.2
GT1A-49Z4 69.5–75.5	Ol Gabbro	26	−0.2	0.08	298	0.8	0.130				324	324		0.7
GT1A-57Z2 42.0–51.0	Ol Gabbro				1			4			1	5	0.75	
GT1A-63Z2 59.0–65.5	Ol Gabbro				26	1.0	0.008	689			26	714	0.96	1.0
GT1A-72Z4 33.0–45.0	Ol Gabbro				17						17	17		
GT1A-79Z1 50.5–59.5	Ol Gabbro				11	1.6					11	11		1.6
GT1A-89Z1 18.0–26.0	Opx-bearing ol gabbro				83	−3.2	0.014	1933	17.1	0.02	83	2016	0.96	−3.2
GT1A-96Z1 15.0–23.0	Ol Gabbro				757	2.2	0.149	19			757	776	0.02	2.2
GT1A-100Z1 45.0–50.0	Ol Gabbro				303	−0.1	0.043	7			303	309	0.02	−0.1
GT1A-107Z2 55.0–62.0	Ol Gabbro				59	2.6	0.009	99			59	157	0.63	2.6
GT1A-112Z2 69.0–77.0	Ol Gabbro				32	1.2	0.017	1			32	33	0.03	1.2
GT1A-119Z4 12.0–20.0	Ol Gabbro	146	0.3	0.02	392	0.6	0.099	113			538	651	0.17	0.5
GT1A-123Z2 0.0–8.0	Ol Gabbro				24	2.3	0.010	1			24	25	0.04	2.3
GT1A-136Z3 29.0–37.0	Ol Gabbro				52	2.3	0.004	2			52	53	0.03	2.3
GT1A-138Z2 56.0–64.0	Ol Gabbro	136	−0.4	0.01	429	0.5	0.114	14			565	579	0.02	0.3
GT1A-141Z4 0.0–8.0	Ol bearing Gabbro				35	1.4	0.005	24	16.1	0.02	35	58	0.41	1.4

(*continued on next page*)

Table 1 (*continued*)

Ref	Lithology	AVS			CRS			Sulfates			Sulfide-S (ppm)	TS Ext (ppm)	SO_4/TS	$\delta^{34}S$ Bulk Sulfide
		S (ppm)	$\delta^{34}S$ (‰)	± (‰)	S (ppm)	$\delta^{34}S$ (‰)	±	S (ppm)	$\delta^{34}S$ (‰)	±(‰)				
GT1A-147Z2 49.0–54.0	Ol bearing Gabbro				114	1.9	0.020				114	114		1.9
GT1A-151Z2 45.0–55.0	Ol Gabbro				306	0.8	0.034	5			306	311	0.02	0.8
GT1A-152Z3 0.0–8.0	Ol Gabbro				310	0.6	0.017	1			310	311	0.00	0.6

Table 2
Multiple sulfur isotope composition extracted from selected bulk rocks.

Ref	Lithology	Δ36S [‰]	Δ33S [‰]	δ34S [‰]
GT3A-26Z3 10.0–15.0	Diabase	1.001	−0.012	5.31
GT3A-41Z3 22.0–27.0	Basalt	1.192	−0.048	−11.37
GT3A-48Z1 11.0–13.0	Basalt	1.069	0.018	13.76
GT3A-56Z1 59.0–64.0	Ol Gabbro	0.931	0.008	13.80
GT3A-63Z1 0.0–6.0	Plag-cpx phyric Basalt	0.986	0.005	14.27
GT3A-100Z4 67.0–72.0	Oxide Gabbro	0.815	−0.002	5.56
GT3A-101Z3 66.0–71.0	Basalt	0.877	−0.008	10.94
GT3A-128Z2 62.0–70.0	Oxide Gabbro	0.968	−0.017	5.33
GT3A-141Z4 43–51	Pyrite Epidote patch	1.069	−0.011	8.91
GT3A-142Z4 61.0–69.0 DIOR	Diorite	0.802	−0.028	5.52
GT3A-146Z1 57.0–65.0	Oxide Gabbro	0.673	−0.007	7.44
GT2A-24Z2 31.0–36.0	Ol gabbro	1.239	−0.042	1.22
GT2A-31Z1 70.0–75.1	Ol gabbro	1.091	−0.036	1.42
GT2A-67Z3 58.0–68.0	Ol gabbro	1.022	−0.029	1.79
GT2A-83Z1 74.5–82.0	Ol-bearing Gabbro	1.520	−0.024	2.28
GT2A-100Z4 44.0–50.0	Ol gabbro	1.059	−0.014	−0.66
GT2A-108Z1 34.0–44.0	Ol-bearing Gabbronorite	0.857	−0.034	2.20
GT2A-133Z3 26.0–33.0	Ol gabbro	0.907	−0.023	0.78
GT1A-30Z1 55.0–60.0	Ol Gabbro	1.145	−0.023	1.55
GT1A-31Z2 20.0–25.0	Ol bearing Gabbro	1.145	−0.033	0.59
GT1A-49Z4 69.5–75.5	Ol Gabbro	1.143	−0.032	0.60
GT1A-100Z1 45.0–50.0	Ol Gabbro	1.083	−0.019	−0.17
GT1A-123Z2 0.0–8.0	Ol Gabbro	1.119	−0.035	2.42
GT1A-147Z2 49.0–54.0	Ol bearing Gabbro	0.980	−0.042	2.03
GT1A-152Z3 0.0–8.0	Ol Gabbro	1.044	−0.030	0.76

were combusted with vanadium pentoxide in tin capsules along with the standards IAEA-S1, —S2, —S3 and NBS127 for calibration. Results are reported in the common δ notation relative to Vienna Canyon Diablo Troilite (V-CDT):

$$\delta^{34}S_{sample} = \left[\left({}^{34}S/{}^{32}S \right)_{sample} \Big/ \left({}^{34}S/{}^{32}S \right)_{V-CDT} - 1 \right] \times 1000. \quad (1)$$

Reproducibility for $\delta^{34}S$ values was better than ±0.3 ‰ (1σ). Whenever no visible amount of H_2S from AVS species was released (i.e. no ZnS precipitate in the vials) CRS was collected subsequently in the same vial and combined with AVS traces for sulfur isotope analysis.

Representative samples were selected for multiple sulfur isotopes (^{32}S, ^{33}S, ^{34}S) measurements using a ThermoScientific Mat 253 mass spectrometer coupled to a fluorination line. Between 2 and 3 mg Ag_2S was converted to SF_6 via fluorination at 300 °C overnight in nickel reactors. SF_6 was cryogenically and chromatographically purified and then introduced into the mass spectrometer via a dual inlet system and masses 127, 128, and 129 (representing ^{32}S, ^{33}S, and ^{34}S, respectively) measured simultaneously (Peters et al., 2011). The IAEA-S1 standard was used as reference material. Following Farquhar et al. (2000), Peters et al. (2010) and Peters et al. (2011) $\Delta^{33}S$ is defined as (Eq. (2)).

$$\Delta^{33}S = \delta^{33}S - 1000 \times \left[\left(1 + \delta^{34}S/1000 \right)^{0.515} - 1 \right] \quad (2)$$

Reproducibility for Δ^{33S} measurements is better than ±0.008 ‰ (1σ).

3.5. In-situ sulfur isotopes

In-situ measurements in pyrite, pyrrhotite and chalcopyrite were performed on sub-sampled portions of previously studied thin sections representative of the three drillholes at the NordSIMS laboratory, Swedish Museum of Natural History, Stockholm. Mounts with the cut fragments were polished, gold coated, and then analyzed for $\delta^{34}S$ using a CAMECA IMS-1280 large-geometry secondary ion mass spectrometer (LG-SIMS). The method broadly followed that described by Whitehouse et al. (2005) and Whitehouse (2013). A 20 keV impact energy, ~6 μm-sized, critically focused beam of $^{133}Cs^+$ ions, rastered over 10 × 10 μm to homogenise the crater base, was used to locally sputter and ionize S from individual pyrite grains. A low energy electron flooding gun was used to prevent charge buildup on adjacent, non-conducting matrix phases and/or inclusions. The ^{32}S and ^{34}S isotopes were separated using an NMR-regulated magnetic field and detected in two Faraday detectors operating at a mass resolution of 2430 (M/ΔM). Matrix matched reference materials were regularly interspersed with the analyses of unknowns and used to determine instrumental mass bias in order to derive the correct values of $\delta^{34}S_{V\text{-}CDT}$. These reference materials were for pyrite Ruttan (Crowe and Vaughan, 1996; recalibrated by Cabral et al., 2013) and S0302A (; Liseroudi et al., 2021); for chalcopyrite Nifty-B (LaFlamme et al., 2016); and for pyrrhotite YP-136 (Li et al., 2019) or MV1 (Whitehouse, 2013). Reproducibility (1 std. deviation) based on the frequent standard measurements in each analytical session (= sample mount) was propagated together with the within run uncertainties to yield the overall uncertainty on $\delta^{34}S$ for a given analysis, as reported in Table 3.

4. Results

4.1. Sulfide mineralogy

Sulfides were classified based on their micro-textures and associated paragenesis. *Magmatic sulfides* form blebs or larger, smooth-surfaced, interstitial aggregates of pyrrhotite with chalcopyrite and pentlandite which occurs as exsolutions or granular aggregates (Fig. 4C). *Remobilized sulfides* are magmatic sulfides that preserve their original mineralogy but were partly replaced by secondary silicates (amphibole, chlorite) during hydrothermal alteration, without formation of secondary sulfide phases. They can be recognized by their ragged edges and the outline of the original aggregate, with some outlined by micron sulfide remnants intergrown with the hydrous silicates (Fig. 4D, E). Newformed sulfides were labelled as *hydrothermal* (Fig. 4G-H) and can be found replacing silicates, magmatic sulfides or in veinlets. Hydrothermal

Table 3
$\delta^{34}S$ values measured in-situ for selected samples.

SAMPLE		Mineral Phase	Sulfide Type	$\delta^{34}S$ ‰	± ‰
GT3A-47Z4 34–39	Basalt	Py small bleb 1 (C)	Hydro	**13.8**	0.05
GT3A-47Z4 34–39	Basalt	Py small bleb 1 (B)	Hydro	**13.9**	0.06
GT3A-47Z4 34–39	Basalt	Py small bleb 2 (C)	Hydro	**13.5**	0.05
GT3A-47Z4 34–39	Basalt	Py small bleb 2 (B)	Hydro	**12.9**	0.06
GT3A-48Z1 11–13	Basalt	Py large bleb (C)	Hydro	**11.9**	0.05
GT3A-48Z1 11–13	Basalt	Py large bleb (T)	Hydro	**11.1**	0.06
GT3A-48Z1 11–13	Basalt	Py large bleb (T)	Hydro	**12.7**	0.08
GT3A-48Z1 11–13	Basalt	Py large bleb (T)	Hydro	**14.2**	0.06
GT3A-48Z1 11–13	Basalt	Py large bleb (B)	Hydro	**14.4**	0.05
GT3A-140Z2 22–30	Basalt	Ccp dusty	Hydro	**2.5**	0.28
GT3A-140Z2 22–30	Basalt	Ccp dusty	Hydro	**1.8**	0.29
GT3A-140Z2 22–30	Basalt	Py large aggregate (C)	Hydro	**1.0**	0.08
GT3A-140Z2 22–30	Basalt	Py large aggregate (C)	Hydro	**0.9**	0.08
GT3A-140Z2 22–30	Basalt	Py large aggregate (C)	Hydro	**1.2**	0.09
GT3A-140Z2 22–30	Basalt	Py large aggregate (B)	Hydro	**0.9**	0.09
GT3A-140Z2 22–30	Basalt	Py large aggregate (B)	Hydro	**0.7**	0.08
GT3A-140Z2 22–30	Basalt	Py grain 2 (C)	Hydro	**−1.0**	0.09
GT3A-140Z2 22–30	Basalt	Py grain 1 (B)	Hydro	**1.0**	0.08
GT3A-140Z2 22–30	Basalt	Py grain 1 (B)	Hydro	**1.2**	0.08
GT3A-141Z4 43–51	Ep Py patch	Py-ep patch ©	Hydro	**9.6**	0.07
GT3A-141Z4 43–51	Ep Py patch	Py-ep patch (traverse)	Hydro	**10.0**	0.07
GT3A-141Z4 43–51	Ep Py patch	Py-ep patch (traverse)	Hydro	**9.3**	0.07
GT3A-141Z4 43–51	Ep Py patch	Py-ep patch (traverse)	Hydro	**9.5**	0.07
GT3A-141Z4 43–51	Ep Py patch	Py-ep patch (traverse)	Hydro	**9.9**	2.00
GT3A-141Z4 43–51	Ep Py patch	Py-ep patch (B)	Hydro	**7.3**	0.07
GT3A-142Z3 4–10	Diorite	Ccp grain 1 (C)	Hydro	**13.1**	0.09
GT3A-142Z3 4–10	Diorite	Ccp grain 1 (B)	Hydro	**2.4**	0.10
GT3A-142Z3 4–10	Diorite	Ccp grain 2 (C)	Hydro	**7.4**	0.11
GT3A-142Z3 4–10	Diorite	Ccp grain 2 (B)	Hydro	**7.2**	0.11
GT3A-142Z3 4–10	Diorite	Ccp small	Hydro	**3.1**	0.15
GT3A-142Z3 4–10	Diorite	Ccp small	Hydro	**6.4**	0.08
GT3A-142Z3 4–10	Diorite	Ccp small	Hydro	**7.4**	0.08
GT3A-142Z3 4–10	Diorite	Py 1 (C)	Hydro	**3.1**	0.08
GT3A-142Z3 4–10	Diorite	Py 1 (B)	Hydro	**5.4**	0.10
GT3A-142Z3 4–10	Diorite	Py 2 (C)	Hydro	**1.6**	0.08
GT3A-142Z3 4–10	Diorite	Py 2 (B)	Hydro	**1.3**	0.09
GT3A-146Z1 57–65	Oxide Gb	Py non cataclastic (C)	Hydro	**6.2**	0.06
GT3A-146Z1 57–66	Oxide Gb	Py non cataclastic (B)	Hydro	**5.9**	0.06
GT3A-146Z1 57–67	Oxide Gb	Py Cataclastic ©	Hydro	**6.0**	0.06
GT3A-146Z1 57–68	Oxide Gb	Py Cataclastic (B)	Hydro	**6.4**	0.07
GT2A-31Z1 68–70	Ol Gabbro	Ccp Vein	Hydro	**0.7**	0.11
GT2A-31Z1 68–70	Ol Gabbro	Ccp Vein	Hydro	**0.4**	0.11
GT2A-31Z1 68–70	Ol Gabbro	Ccp Vein	Hydro	**1.5**	0.12
GT2A-36Z1 59–62	Ol Gabbro	Ccp (C)	Remob	**1.2**	0.10
GT2A-36Z1 59–62	Ol Gabbro	Ccp (B)	Remob	**1.3**	0.10
GT2A-36Z1 59–62	Ol Gabbro	Py after Po (C)	Metas	**−1.5**	0.33
GT2A-36Z1 59–62	Ol Gabbro	Py after Po (B)	Metas	**−0.8**	0.27
GT2A-36Z1 59–62	Ol Gabbro	Ccp in altered Ol (C)	Remob	**0.8**	0.12
GT2A-36Z1 59–62	Ol Gabbro	Py bulky (C)	Hydro	**0.1**	0.11
GT2A-36Z1 59–62	Ol Gabbro	Py bulky (B)	Hydro	**1.6**	0.13
GT2A-100Z4 14–17	Ol Gabbro	Ccp intergranular veinlet (C)	Hydro	**0.6**	0.19
GT2A-100Z4 14–17	Ol Gabbro	Ccp intergranular veinlet (B)	Hydro	**0.4**	0.16
GT2A-100Z4 14–17	Ol Gabbro	Ccp Pl fractures	Hydro	**1.0**	0.16
GT2A-100Z4 14–17	Ol Gabbro	Ccp Ol fractures	Hydro	**0.7**	0.19
GT2A-100Z4 14–17	Ol Gabbro	Ccp intergranular veinlet	Hydro	**−1.8**	0.23

(*continued on next page*)

Table 3 (*continued*)

SAMPLE		Mineral Phase	Sulfide Type	$\delta^{34}S$ ‰	± ‰
GT2A-100Z4 14–17	Ol Gabbro	Ccp Ol fractures	Hydro	**1.6**	0.16
GT2A-100Z4 14–17	Ol Gabbro	Py dendritic aggregate (C)	Hydro	**2.7**	0.11
GT2A-100Z4 14–17	Ol Gabbro	Py dendritic aggregate (B)	Hydro	**1.6**	0.06
GT2A-100Z4 14–17	Ol Gabbro	Ccp in hydrous silicates (C)	Meta	**1.1**	0.19
GT2A-100Z4 14–17	Ol Gabbro	Ccp in hydrous silicates (B)	Meta	**1.8**	0.15
GT2A-139Z4 77–80	Ol Gabbro	Ccp	Remob	**0.0**	0.13
GT2A-139Z4 77–80	Ol Gabbro	Po (C)	Remob	**−1.8**	0.15
GT2A-139Z4 77–80	Ol Gabbro	Po (B)	Remob	**−3.8**	0.19
GT2A-139Z4 77–80	Ol Gabbro	Po Smec-Chl aggregate after Ol	Hydro	**−3.8**	0.17
GT2A-139Z4 77–80	Ol Gabbro	Po Smec-Chl aggregate after Ol	Hydro	**−3.8**	0.12
GT2A-139Z4 77–80	Ol Gabbro	Po Smec-Chl aggregate after Ol	Hydro	**−5.0**	0.24
GT2A-139Z4 77–80	Ol Gabbro	Py dendritic aggregate (C)	Hydro	**−1.0**	0.12
GT2A-139Z4 77–80	Ol Gabbro	Py dendritic aggregate (C)	Hydro	**−1.2**	0.11
GT1A-30Z1 55–60	Ol Gabbro	Ccp in Polydimite aggregate	Meta	**1.4**	0.07
GT1A-30Z1 55–60	Ol Gabbro	Ccp	Remob	**0.5**	0.10
GT1A-30Z1 55–60	Ol Gabbro	Ccp	Remob	**0.6**	0.09
GT1A-30Z1 55–60	Ol Gabbro	Ccp in altered Ol	Hydro	**2.0**	0.09
GT1A-30Z1 55–60	Ol Gabbro	Ccp in altered Ol	Hydro	**1.0**	0.13
GT1A-31Z2 20–25	Ol bearing Gabbro	Ccp in Po	Mag	**0.9**	0.06
GT1A-31Z2 20–25	Ol bearing Gabbro	Ccp in Po	Mag	**0.9**	0.06
GT1A-31Z2 20–25	Ol bearing Gabbro	Ccp in Po	Mag	**0.9**	0.07
GT1A-31Z2 20–25	Ol bearing Gabbro	Ccp in Po	Mag	**1.0**	0.08
GT1A-31Z2 20–25	Ol bearing Gabbro	Ccp in Po	Mag	**0.8**	0.07
GT1A-31Z2 20–25	Ol bearing Gabbro	Po	Mag	**0.0**	0.10
GT1A-31Z2 20–25	Ol bearing Gabbro	Po	Mag	**0.1**	0.10
GT1A-31Z2 20–25	Ol bearing Gabbro	Po	Mag	**0.0**	0.09
GT1A-31Z2 20–25	Ol bearing Gabbro	Po	Mag	**−1.0**	0.79
GT1A-31Z2 20–25	Ol bearing Gabbro	Po Smec-Chl aggregate after Ol	Hydro	**0.5**	0.10
GT1A-31Z2 20–25	Ol bearing Gabbro	Po Smec-Chl aggregate after Ol	Hydro	**0.8**	0.10
GT1A-72Z4 33–45	Ol Gabbro	Ccp platelets in Cpx	Hydro	**0.5**	0.10
GT1A-72Z4 33–45	Ol Gabbro	Ccp platelets in Cpx	Hydro	**2.5**	0.07

Table 3 (*continued*)

SAMPLE		Mineral Phase	Sulfide Type	$\delta^{34}S$ ‰	± ‰
GT1A-72Z4 33–45	Ol Gabbro	Ccp platelets in Cpx	Hydro	**−1.2**	0.13
GT1A-72Z4 33–45	Ol Gabbro	Ccp platelets in Cpx	Hydro	**−0.4**	0.22
GT1A-100Z1 45–50	Ol Gabbro	Ccp	Remob	**−0.3**	0.13
GT1A-100Z1 45–50	Ol Gabbro	Ccp	Remob	**−0.4**	0.12
GT1A-100Z1 45–50	Ol Gabbro	Py after Po	Meta	**−3.2**	0.29
GT1A-100Z1 45–50	Ol Gabbro	Py in Ccp aggregagte	Metas	**0.4**	0.07
GT1A-100Z1 45–50	Ol Gabbro	Py in Ccp aggregagte	Metas	**0.0**	0.08
GT1A-100Z1 45–50	Ol Gabbro	Ccp in Py aggregate	Remob	**0.1**	0.11
GT1A-112Z2 69–77	Ol Gabbro	Co-pyrite (C)	Hydro	**2.2**	0.08
GT1A-112Z2 69–77	Ol Gabbro	Co-pyrite (B)	Hydro	**2.6**	0.08
GT1A-112Z2 69–77	Ol Gabbro	Co-pyrite (B)	Hydro	**1.5**	0.08
GT1A-152Z3 0–8	Ol Gabbro	Ccp in Po anomalous	Mag	**−0.8**	0.12
GT1A-152Z3 0–8	Ol Gabbro	Po bleb	Mag	**−2.2**	0.10
GT1A-152Z3 0–8	Ol Gabbro	Po bleb	Mag	**−4.3**	0.14

sulfides that can be identified as partially or totally replacing preexisting magmatic sulfide assemblages were further sub-divided as hydrothermal- *metasomatic* (Fig. 4F).

Fig. 5 shows the relative vol% of magmatic, remobilized and hydrothermal (including metasomatic) sulfides in a composite downhole plot. Sulfides from the dike-gabbro transition zone (Hole GT3A) are scarce only exceeding 1 %vol on few intervals: 97–120, 222.8, 253–258 m and in the lowermost ~42 m (357.6 to 375 m; **Fig. 5**A). The most strongly sulfide mineralized interval is a pyrite-epidote patch at 362.2 m in the Lower Gabbro Sequence (Fig. 3D). All sulfides identified are hydrothermal except for within a diabase at 6.6 m (sample GT3 A-9Z-1 7–12 cm) where minute fragments of pyrrhotite are preserved within amphibole replacing clinopyroxene. Sulfide blebs are common at the contacts between (glassy) basalt crosscutting gabbro or diorite. Within the Upper Dike sequence some blebs are large, up to 1–3 mm (Fig. 3A-**A1**) whereas in the Lower Dike and Gabbro sequences they form arrays bordering lithological contacts (Fig. 3B). The blebs correspond to porous/spongy pyrite aggregates overgrowing the altered matrix and their shape and mode of occurrence strongly suggests they are the result of pseudomorphic replacement of preexisting magmatic sulfides. Pyrite dominates the sulfide assemblage down to ~300 m, most commonly as small porous/spongy grains overgrowing the intensely altered silicate assemblage, and more rarely as shattered crystals within cataclastic bands. Pyrite in Hole GT3A is close to an ideal composition (Fig. 6A-B), with minor elevated Co concentration relative to other analyzed metals (Fig. 6C). Chalcopyrite is rare and occurs as small granular or dusty aggregates and becomes more abundant below ~300 CCD (Fig. 3C),

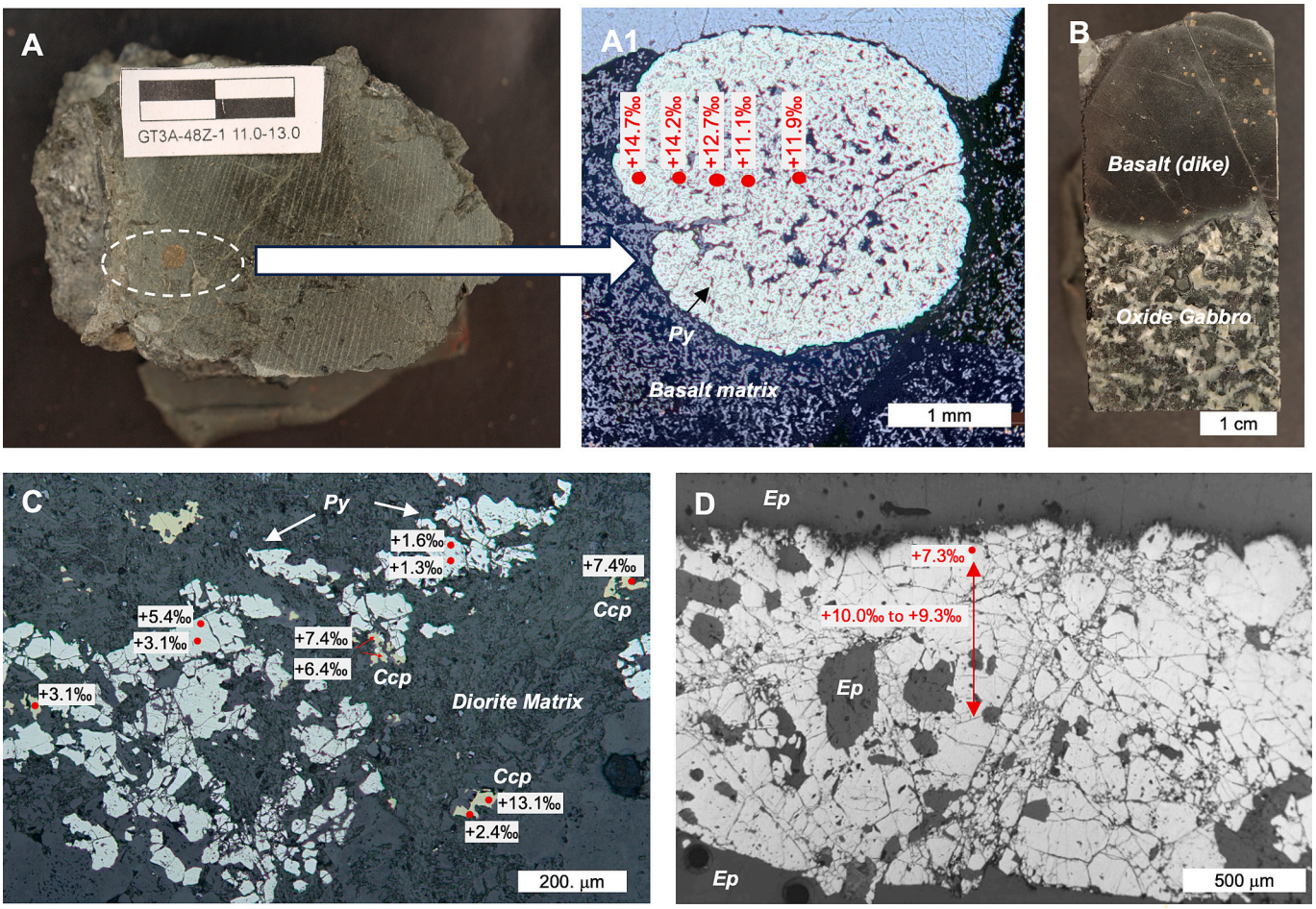

Fig. 3. Hole GT3A sulfide mineralogy with spots showing locations of SIMS analyses. **(A-A1)** Basalt with large magmatic bleb replaced by pyrite (GT3A-48Z-1 11–13 cm, Upper Dike; 97 m). **(B)** Basalt in dike crosscutting oxide gabbro (GT3-101Z-3 66–71 cm, Lower Gabbro- 254 m) with multiple magmatic blebs replaced by pyrite *(Py)*. **(C)** Pyrite – chalcopyrite *(Ccp)* in diorite (GT3-142Z-3 4–10 cm; Lower Gabbro- 364 m). **(D)** Pyrite-epidote patch in gabbro, (GT3-141Z-4 61–69 cm; Lower Gabbro- 362 m).

commonly associated with epidote. Some chalcopyrite is altered to bornite.

Holes GT1A and GT2A have low sulfide abundances (<< 1 %vol) compared to Hole GT3A cores but wider phase and textural variance (Fig. 5B-D). Magmatic sulfides (as described above) are predominantly preserved in the least altered and deformed intervals (Fig. 5B-D). The foliated gabbros in Hole GT2A have less well preserved pentlandite and more abundant chalcopyrite compared to Hole GT1A, although it is unclear whether this results from remobilization or is a primary feature. In both Holes, sulfides are completely remobilized in intervals with intense cataclastic deformation and hydrothermal overprint, including zones with abundant deformation-related veins and fault gouges. Fault zones are abundant in both Holes GT1A and GT2A but more common in the former where several meter-scale intervals of damaged rock are present (Fig. 5B). Consequently, sulfides are chiefly absent throughout large intervals of Hole GT1A, including those corresponding to the projected intersection of the ZMFZ (~150–100 m). Moderately altered rocks display variable degrees of magmatic sulfide remobilization and deposition of hydrothermal assemblages. In Hole GT1A the most common metasomatic replacement is the formation of pyrite-millerite ±chalcopyrite, whereas pyrite + siegenite-polydimite$_{ss}$ ± chalcopyrite aggregates are more common in Hole GT2A (Fig. 4D, F; Fig. 5A-B). Pyrite can also form idiomorphic or blocky aggregates overgrowing the silicate assemblage that are more abundant as pyrrhotite disappears from the assemblage (Fig. 4G). Minute aggregates of sphalerite are more common in Hole GT2A, mostly associated with hydrothermal chalcopyrite although some partially fill clinozoisite-albite-chalcopyrite veins (Fig. 4H). Sulfides also show some compositional differences between both Holes. Pyrite tends to be consistently more enriched in both Ni and Co in Hole GT1A relative to Hole GT2A (Fig. 6C) whereas magmatic pyrrhotite tends to show minor (<1 wt%) enrichment in Ni leading to Ni/Co ratios >1 (Fig. 6C). Pyrrhotite platelets in smectite-chlorite pseudomorphs after olivine (Fig. 4A-B) show similar metal contents relative to its magmatic counterparts, although some pyrrhotite grains in Hole GT2A display a low Ni/Co trend similar to pyrite (Fig. 6C).

4.2. Bulk rock sulfur contents and isotope compositions

Results for extracted sulfide sulfur and sulfate contents are presented in Table 1 and plotted in a composite downhole profile in Fig. 7. Fig. 8 shows the statistical distribution for the total sulfide sulfur concentrations and isotope compositions.

Sulfur contents ($TS_{sulfide}$) in Hole GT3A show a broad variation with several domains showing very high sulfide concentrations up to 24,902 ppm for a pyrite-epidote patch, but relatively low median values due to very low S concentrations in many studied core intervals (Hole GT3A: X = *median* = 178 ppm, σ = standard deviation = 4873 ppm). Sulfur contents ($TS_{sulfide}$) in the mid- to lower crustal section are higher in Hole GT2A (X = 454 ppm, σ = 693 ppm, max = 2951 ppm) relative to the layered gabbros in Hole GT1A (X = 114 ppm, σ = 277 ppm, max = 1050 ppm).

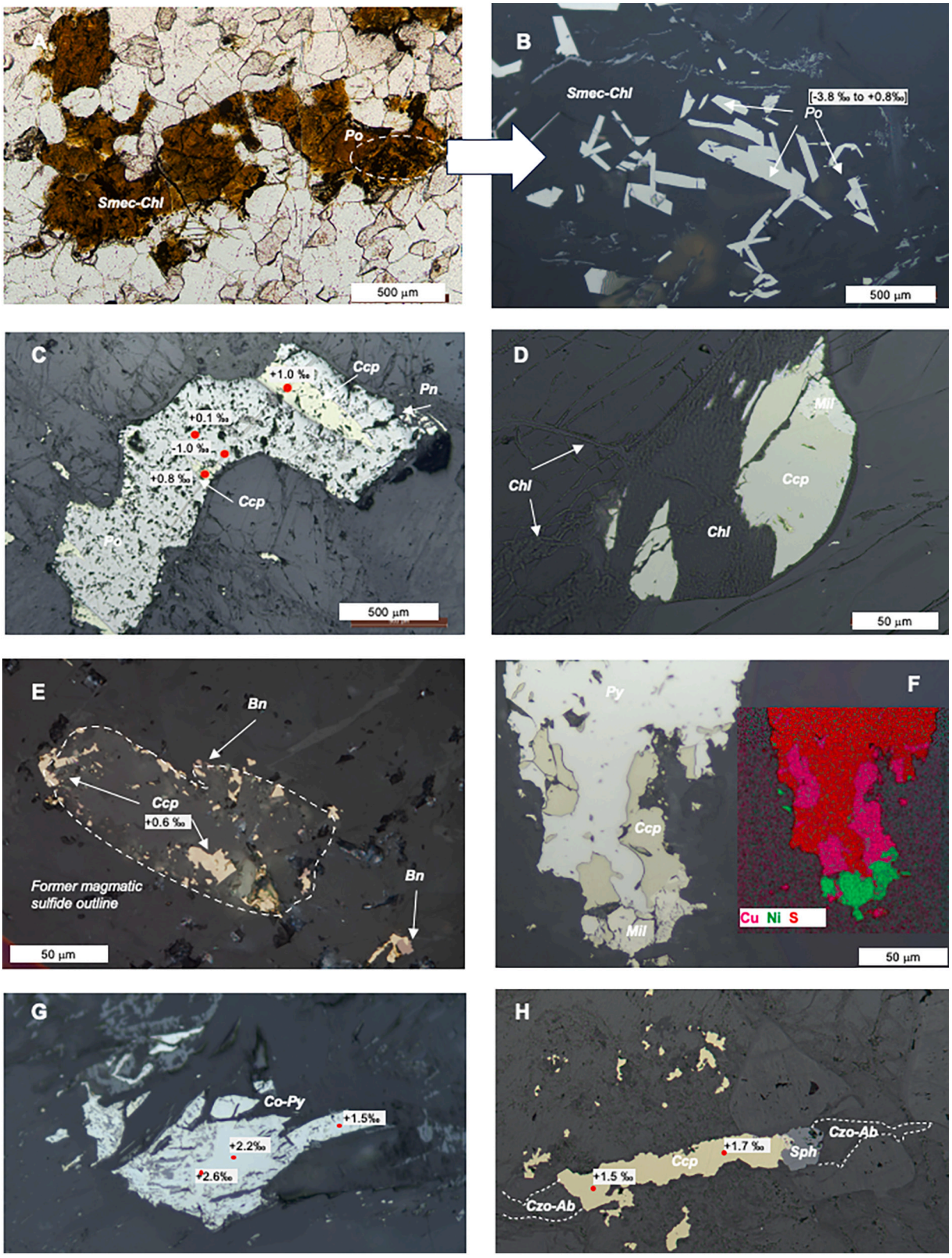

Fig. 4. Sulfide mineralogy in Holes GT1A and GT2A with spots showing location of SIMS analyses **(A-B)** Smectite-chlorite (*Smec-Chl*), replacing olivine enclosing pyrrhotite *(Po)* platelets (GT2-45Z1 32–35 cm; 117.6 m). **(C)** Magmatic sulfide pyrrhotite - chalcopyrite (*Ccp*) – pentlandite (remobilized- *Pn*) (GT1-31Z-2 20–25 cm; 73.9 m). **(D)** Metasomatic sulfide chalcopyrite – millerite (*Mil*) replaced by chlorite (*Chl*) (GT2–100Z-4 14–17 cm; 270.4 m); **(E)** Remobilized sulfide with chalcopyrite remnants, partly oxidized to bornite (*Bn*) (GT1-30Z-1 55–60 cm; 70.4 m); **(F)** Metasomatic sulfide pyrite-millerite-chalcopyrite showing EDS compositional map (GT2-55Z2 63–65 cm; 147.4 m); **(G)** Hydrothermal chalcopyrite-sphalerite (*Sph*) vein with albite (*Ab*) and clinozoisite (*Czo*) (GT2A-31Z-1 68–70 cm; 76 m).

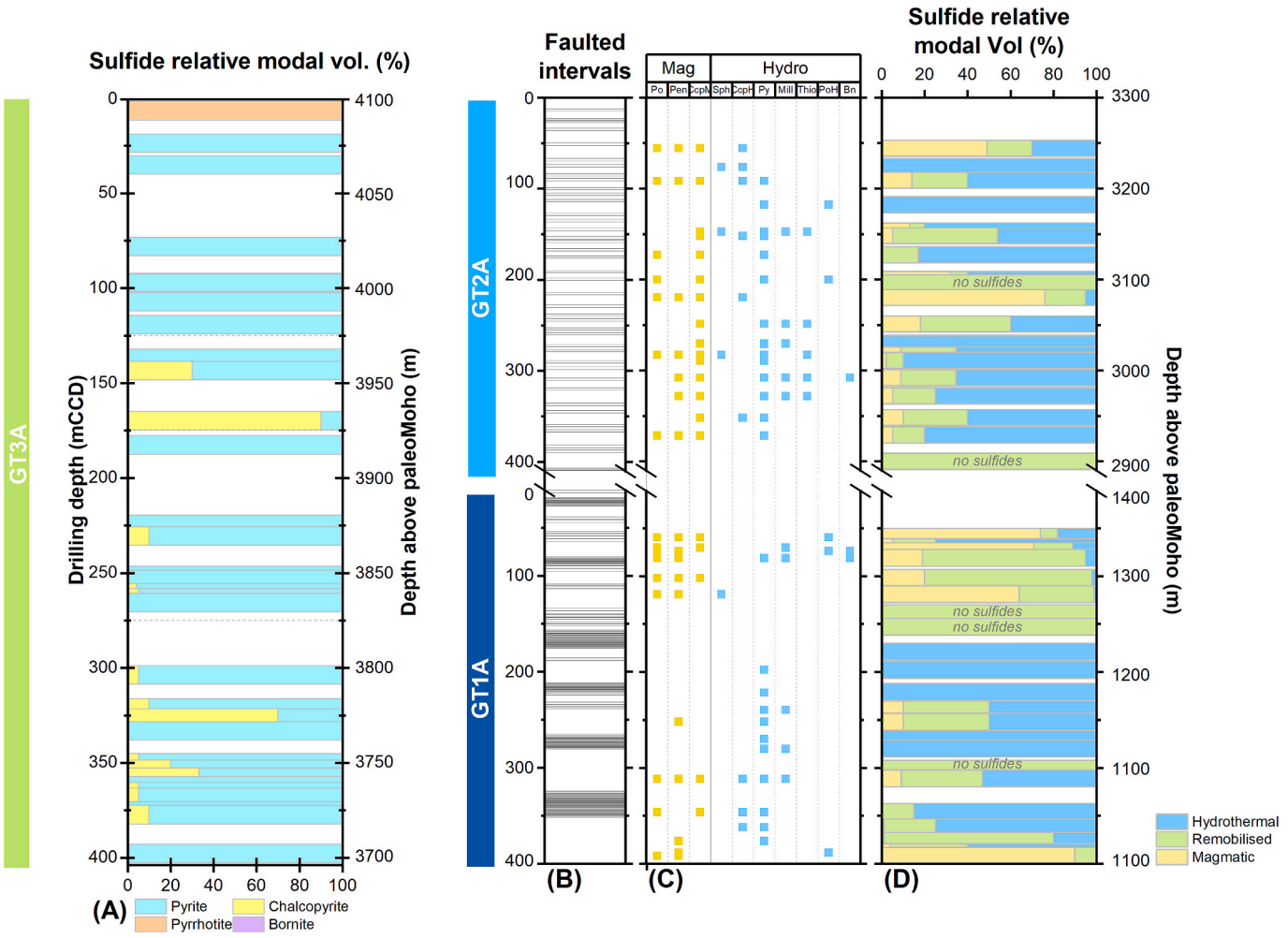

Fig. 5. Sulfide mineralogy variations with depth. **(A)** Hole GT3A relative modal volume % of sulfide. With the exception of the uppermost sample, all sulfides are hydrothermal. **(B—D)** Hole GT1A and GT2A showing: **(B)** Faulted intervals, **(C)** Individual sulfide minerals, shown as present or absent since modal amounts are very low and, **(D)** relative modal volume sulfides (%) shown for magmatic vs. remobilized or hydrothermal (including metasomatic, see text). Abbreviations: *Mag*- magmatic, *Hydro*- hydrothermal *Po*- pyrrhotite, *Pn*-pentlandite, *Ccp*- chalcopyrite, *Sph*- sphalerite, *Py*- pyrite, *Mil*- millerite, *Thi*- thiospinels (polydymite- siegenite$_{ss}$), *Bn*- bornite. All depth scales in m-CCD (*Chikyu Curated Depth* as in Kelemen et al., 2020).

Samples from Hole GT3A only yielded CRS with a wide range in $\delta^{34}S$ from −12.8 ‰ to +13.6 ‰. Isotope variations are not lithology-dependent but show distinct variations with depth: samples down to ~80 m vary from −12.8 ‰ to +5.1 ‰ and generally have very low $TS_{sulfide}$ contents. From 80 m $\delta^{34}S$ reaches its highest value ($\delta^{34}S$ = +13.6 ‰), and then broadly decreases downhole, albeit not uniformly and is associated with widely variable $TS_{sulfide}$ concentrations (Fig. 7). Pyrrhotite is scarce in Hole GT2A and only traces of AVS were recovered, insufficient for isotope measurements. In Hole GT1A, the AVS fraction ($\delta^{34}S_{AVS}$ = −0.4 ‰ to +1.9 ‰) lies within ~1 ‰ relative to the isotope composition of the coexisting CRS fraction ($\delta^{34}S_{CRS}$ = −3.2 ‰ to +2.6 ‰). The median $\delta^{34}S$ for CRS fraction in both mid- to lower crustal holes is identical (X = +1.2 ‰) with Hole GT1A samples spanning a slightly wider range of compositions ($\delta^{34}S$ = −3.2 ‰ to +2.6 ‰) relative to Hole GT2A ($\delta^{34}S$ -0.7 ‰ to +2.1 ‰).

The relationships between sulfate and sulfide are shown in Fig. 9. Sulfate minerals are scarce throughout the Wadi Gideah drill holes with similar median concentration values for the entire studied crustal section (X ~ 10–12 ppm) and sulfate is generally only a small fraction of the extracted total sulfur, with TS_{SO4}/TS_{ext} mostly <0.2 (Fig. 9B). Maximum sulfate concentrations increase from Hole GT3A (76 ppm), to Hole GT2A (197 ppm) to 1933 ppm in fault zone samples from Hole GT1A, that also include traces of pyrite. The $\delta^{34}S$ isotope composition for sulfates is generally close to the range of coexisting sulfides, except for three GT1A and GT2A samples with higher sulfate fractions (TS_{SO4}/TS_{ext} 0.40 to 0.96). Here, sulfate with a $\delta^{34}S$ value up to +17.3 ‰, is considerably higher than the coexisting sulfides.

4.2.1. *Multiple sulfur isotope compositions*

Multiple sulfur isotope measurements performed on CRS extracts for selected samples are listed in Table 2 and shown in Fig. 7C; Fig. 10 shows respective $\Delta^{33}S$ and $\delta^{34}S$ values. Mid-lower crustal rocks show uniformly negative $\Delta^{33}S$ compositions (Hole GT1A = −0.042 ‰ to −0.019 ‰; GT2A = −0.042 ‰ to −0.014 ‰), that display a near vertical trend with $\delta^{34}S$. Hole GT3A has one sample with a very negative $\Delta^{33}S$ value of −0.048 ‰ and a $\delta^{34}S$ value of −12.8 ‰, but other Hole GT3A samples have $\Delta^{33}S$ between −0.028 ‰ to +0.018 ‰ and display a steep positive trend with $\delta^{34}S$ (Fig. 10).

4.3. *In-situ isotope compositions*

In-situ SIMS data are listed in Table 3, with point locations for representative mineral assemblages shown in Fig. 4. In-situ measurements in the dike-gabbro transition zone samples (Hole GT3A) aimed to assess the existence of compositional zonings in large hydrothermal sulfide grains and fractionations between different sulfide phases. The

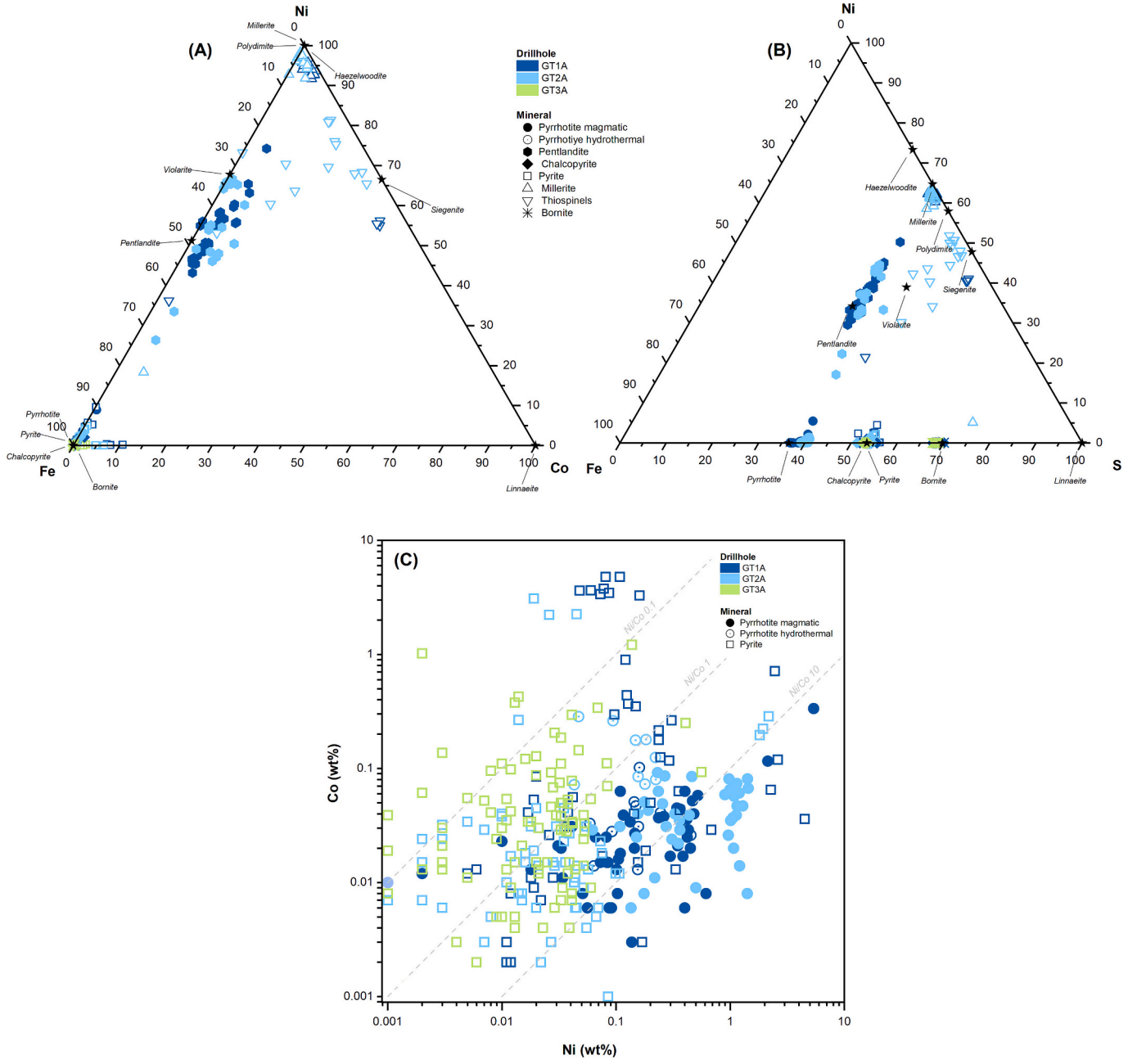

Fig. 6. Sulfide compositional variations. **(A, B)** Fe-Ni-Co and Fe-Ni-S showing endmember compositions (stars) and using wt%. The diagrams show the deviation from ideal compositions in pentlandite towards higher Ni/Fe due to the formation of millerite in both GT1A and GT2A and of violarite-siegenite-polydymite$_{ss}$ in Hole GT2A. Also, it shows that GT3A pyrite-chalcopyrite-bornite hydrothermal assemblages are close to ideal compositions. **(C)** Ni—Co variations for Fe-sulfide phases. EPMA data are available in SM 2 Table 2.

large blebs in basalt samples in the Upper Dike Sequence display lighter sulfur isotope values in their cores relative to grain borders, ranging from +11.9 ‰ to +14.4 ‰ in the largest grains (**Figure 3A1**). In contrast, the epidote-pyrite patch with spongy texture within the Lower Gabbro Sequence (Fig. 3D) shows mostly uniform $\delta^{34}S$ values (+9.3 ‰ to +10.0 ‰) with a single value of +7.3 ‰ in one grain boundary. In the Lower Gabbro Sequence, chalcopyrite is more abundant, and has a heavier isotope composition relative to associated pyrite: one basalt (232 m-CCD) includes pyrite with $\delta^{34}S$ between −1.0 ‰ and + 1.2 ‰ whereas chalcopyrite displays $\delta^{34}S$ values from +1.8 ‰ to 2.5 ‰. This chalcopyrite is partly altered to bornite that was not analyzed due to the lack of appropriate standards. Sulfides in one diorite sample show heterogenous compositions, with significantly higher chalcopyrite $\delta^{34}S$ values (+2.4 ‰ to +13.1 ‰) compared to pyrite (+1.3 ‰ to 5.4 ‰; Fig. 3C). There are no significant differences between cataclastic pyrite and non-cataclastic spongy pyrite in the same samples.

In the mid-lower crust (Holes GT1A and 2A), SIMS analyses focused on distinguishing the composition of mineral species occurring in different paragenetic contexts (see Section 4.2). Median $\delta^{34}S$ values for hydrothermal pyrite (X = +1.6 ‰; −1.2 ‰ to +2.7 ‰) are slightly more positive than for metasomatic pyrite (X = -0.8 ‰; −3.2 ‰ to 0.4 ‰). Magmatic pyrrhotite grains have a slightly negative isotope composition (X = −0.5 ‰; −4.3 ‰ to +0.1 ‰), a tendency more pronounced in grains that experienced remobilization (X = -2.8 ‰; −3.8 ‰ to −1.8 ‰) and hydrothermal pyrrhotite in smectite-chlorite aggregates (X = -3.8 ‰; −5 ‰ to +0.8 ‰). Magmatic, remobilized and hydrothermal

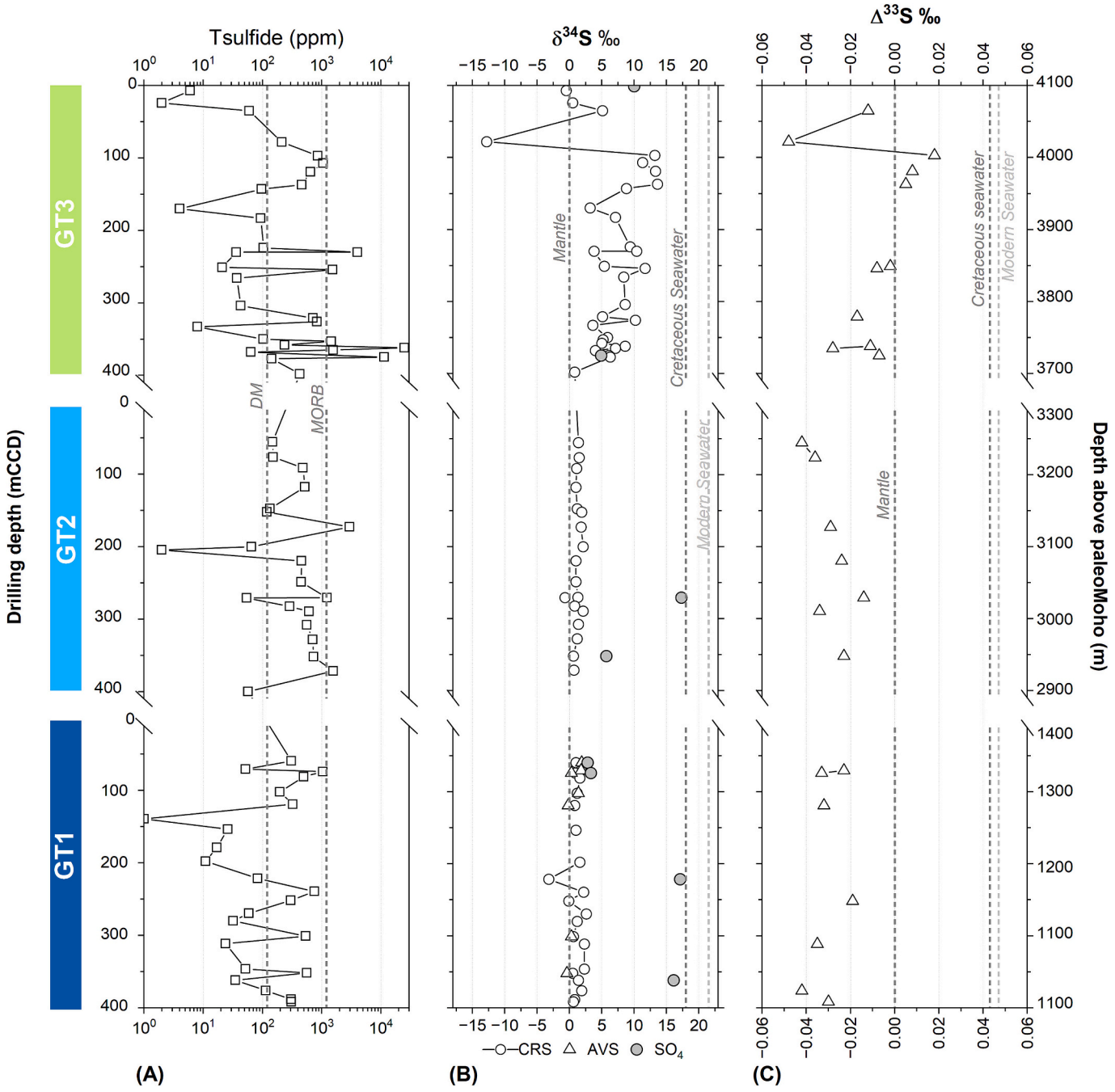

Fig. 7. Downhole variation of whole-rock measurements for a reconstituted stratigraphic section of the three drillholes sulfide sulfur: **(A)** Total sulfide sulfur ($TS_{Sulfide}$); **(B)** $\delta^{34}S$ for sulfide and sulfate fractions; **(C)** $\Delta^{33}S$ in CRS extracts. Also shown for reference: (A) sulfur contents for EPR lavas (Alt et al., 2010) and depleted mantle (DM- Salters and Stracke, 2004); (B) $\delta^{34}S$ for MORB (Sakai et al., 1984), Cretaceous (Kampschulte and Strauss, 2004) and modern seawater (Johnston et al., 2014); (C) $\Delta^{33}S$ for mantle (Labidi et al., 2012; Ono et al., 2007), modern and Cretaceous seawater (Masterson et al., 2016).

chalcopyrite overlap in composition with median values of +0.9 ‰, +0.5 ‰ and + 0.7 ‰ respectively, with a wider spread of values for the hydrothermal chalcopyrite (−1.8 ‰ to +2.5 ‰). Grains representing metasomatic replacement have a slightly heavier isotopic compositions ($X = +1.4$ ‰) although only 3 spots were analyzed showing a relatively narrow compositional range.

As can be seen from Table 3, results from in-situ analyses fall within the range of whole-rock measurements in the same sample or in adjoining domains. There are two noticeable exceptions. Sample GT3A-140Z-2 22–30 cm is a basalt from the Hole GT3A Lower Gabbro Sequence for which in-situ measurements yielded relatively lighter compositions (−1 to +2.5 ‰) compared to the whole rock (+5 ‰). This sample has bornite after chalcopyrite which may have contributed to the heavier composition measured in whole rock. The second disparity occurs in lower crust sample GT1A-152Z-3 0–8 cm where SIMS measurements in pyrrhotite blebs yield negative isotope values (−4.3 ‰ to −2.2 ‰) lower than the measured whole-rock value (0.6 ‰). This sample is essentially fresh and devoid of hydrothermal sulfides therefore the only explanation we can provide is that pyrrhotites are anomalous and/or pentlandite contributed to this sample positive whole-rock isotope signature.

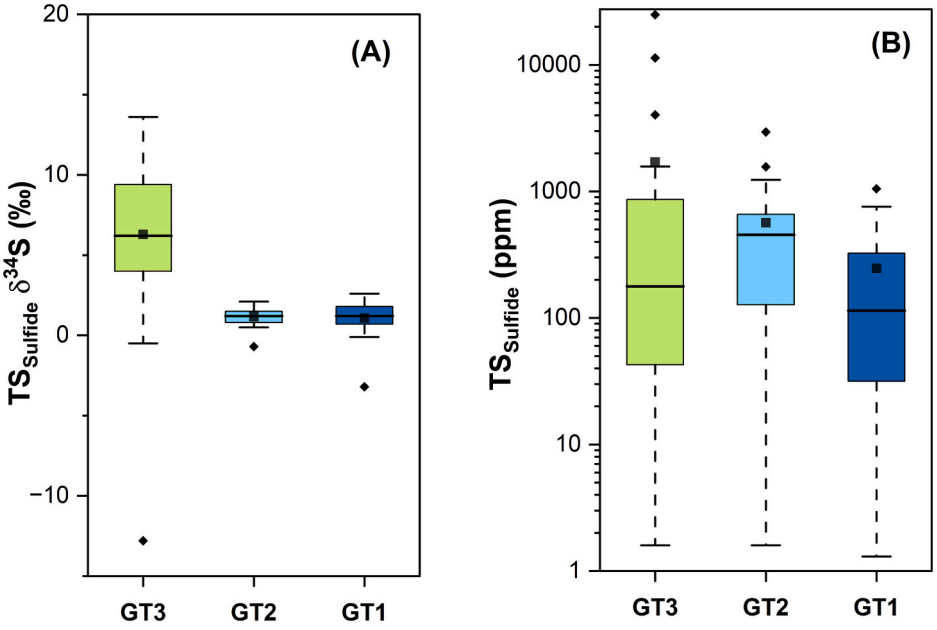

Fig. 8. Statistical distribution of $\delta^{34}S_{TS}$ **(A)** and sulfide-sulfur concentration (i.e. $TS_{sulfide}$ = AVS + CRS) (B) for the three Holes. Upper and lower dashed bars: 95th and 5th percentiles, boxes: 75th and 25th percentiles; thick horizontal bar: median; white squares: mean; diamonds: outliers.

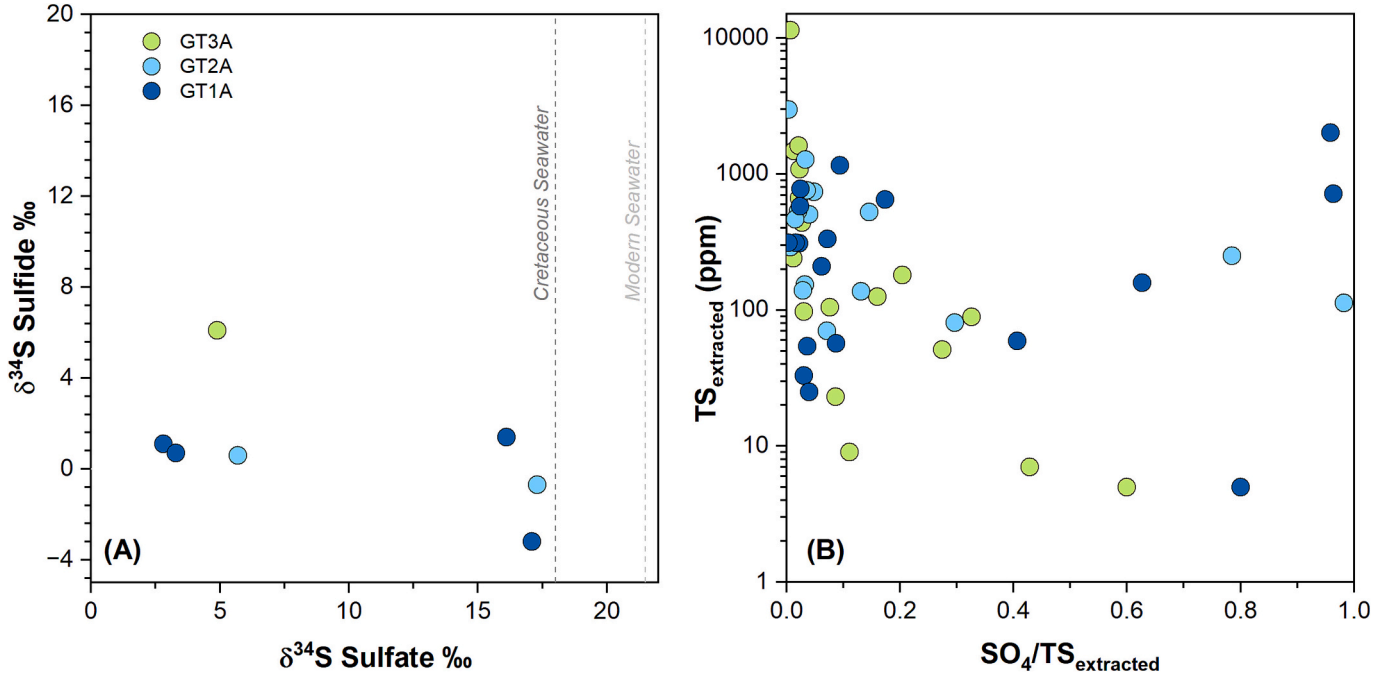

Fig. 9. (A) Relationships between coexisting sulfide and sulfate isotope compositions. **(B)** Total extracted sulfur ($TS_{extracted}$) versus sulfate fraction (TS_{SO4}). Also shown for reference: $\delta^{34}S$ for Cretaceous (Kampschulte and Strauss, 2004) and modern seawater (Johnston et al., 2014).

5. Discussion

5.1. Sulfur geochemistry in the oceanic crust

We firstly evaluate the $\delta^{34}S$ values with respect to sulfur contents in our samples and compare them to well-studied sections of ophiolitic and in-situ oceanic crust (Fig. 11). A first insight into the processes that affected the studied crustal section shows the compositional fields for sulfides formed through different pathways during seawater/rock interaction following Alt et al. (2007). The crustal section is highly heterogenous and includes gabbroic cumulates from the mid-lower crust (Holes GT1A and GT2A) and dikes and varitextured gabbros (Hole GT3A) from the dike-gabbro transition which lithological nature must be considered to determine reference values for primary (magmatic) S concentrations, as discussed below.

5.1.1. Main processes at the dike gabbro transition: Hole GT3A

Sulfide contents in Hole GT3A samples are extremely low considering the non-cumulate, and relatively evolved nature of these rocks (#Mg = Mg/Mg + Fe, molar: $X = 0.53$; 0.32–0.75). Sulfur solubility in basaltic melts increases with Fe content, and variably complex formulation has been proposed to predict sulfur contents in the melt or sulfur

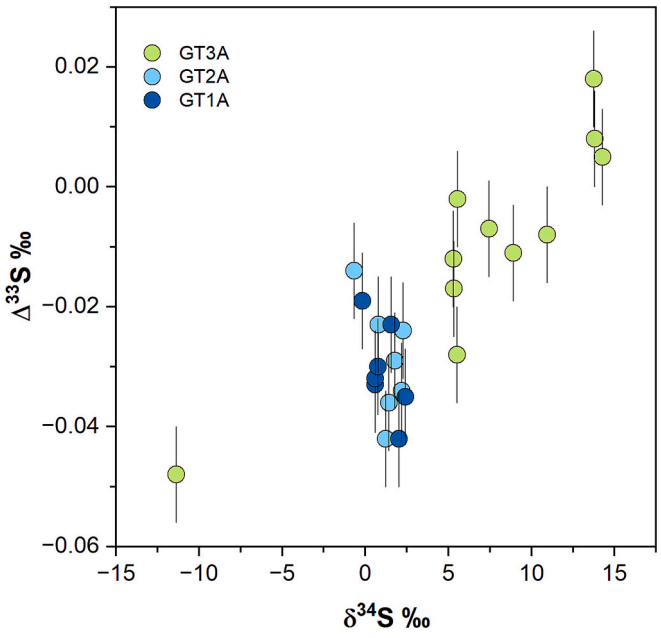

Fig. 10. Relationship between $\Delta^{33}S$ and $\delta^{34}S$ obtained from CRS fractions.

capacity at sulfide saturation-SCSS (Li and Ripley, 2009; Liu et al., 2007; Mathez, 1976). In the absence of S measurements for fresh lavas or glasses from Oman, we rely on #Mg-S relationships (Eq. (3)) for ODP Hole 1256D fresh glasses (Alt and Shanks, 2011) with similar compositional range (#Mg $X = 0.62$; 0.32–0.63), to estimate primary sulfur contents for Hole GT3A samples.

$$S = -0.198\,Mg\# + 0.234 \quad (3)$$

Magmatic sulfur contents for Hole GT3A rocks are estimated to lie between 851 and 1716 ppm, which is significantly higher than their $TS_{Sulfide}$ or TS_{Ext} sulfur contents (Fig. 9, Fig. 11; Supplementary Material SM3- Table 1), implying that pervasive sulfur losses occurred throughout the section. Sulfide additions are concentrated in the Upper Gabbro sequence (~230–250 m) and at the bottom (~360–375 m) of the Lower Gabbro Sequence.

The reduction of seawater sulfate to sulfide via biogenic (Microbial Sulfate Reduction- MSR), or abiogenic high temperature thermochemical sulfate reduction (TSR) pathways will lead to sulfide addition with extensive isotope fractionations. Because of the biological preference for ^{32}S, open system MSR will have large fractionation factors that will lead to very negative isotopic signatures (Canfield, 2004). Only one sample in the Upper Dike Sequence of Hole GT3A has a negative isotope signature −12.8 ‰ consistent with a biogenic origin via MSR. Likewise, one lava sample from Wadi Gideah was reported by Oeser et al. (2012) with a strongly negative $\delta^{34}S$ value of −31.2 ‰. For both samples, sulfur contents are low (~210 ppm) suggesting that these rocks experienced leaching of magmatic sulfur prior to the addition of a small amount of biogenic sulfur. All other upper crust samples in this study show increasingly heavy sulfur isotope signatures at increasing sulfur contents consistent with abiogenic TSR reactions during intense hydrothermal alteration. TSR is most effective above 250 °C, requiring H^+ provided by the simultaneous oxidation of ferromagnesian magmatic minerals in the rock and will lead to moderately heavy $\delta^{34}S$ values (Shanks et al., 1981; Fig. 11). Sulfur isotope values determined here for the dike-gabbro transition (Hole GT3A) section differ substantially from those reported by Oeser et al. (2012). They obtained $\delta^{34}S_{CRS}$ for sulfide between +0.3 to +5.4 ‰ that coexist with heavy sulfates (+2.8 to +14.8 ‰), which fall within the range of our sulfide isotopic compositions (−0.5 to +13.6 ‰; Fig. 11). Given the coincidence between sulfate isotopic values collected in outcrop (Oeser et al., 2012) and sulfide obtained in core samples (this work), we suggest that the surface pyrite sulfur (CRS) may have experienced subaerial oxidation, as is commonly observed in VMS deposits of Oman, where pyrite oxidizes almost immediately after exposure (Cravinho et al., 2023). Oxidation via both abiotic or microbial pathways has been recognized to produce fractionations up to −18 ‰ (Alt et al., 2007; Canfield, 2001; Delacour et al., 2008a; Delacour et al., 2008b). However, it is common that abiotic oxidation results in negligible fractionation thus explaining the overlapping sulfide (this work) and sulfate (Oeser et al., 2012) isotope signatures. Hole GT3A rocks have a remarkably heavy isotopic composition compared to in-situ oceanic crust, consistent with the sheeted dike complex in Cretaceous Troodos ophiolite (Alt, 1994), albeit that the Samail sheeted dikes are even heavier. This is particularly significant considering that Cretaceous seawater was isotopically lighter (Kampschulte and Strauss, 2004; see below) than modern day seawater. Consequently, scenarios of restricted closed system seawater circulation that can produce significantly heavier isotope signatures will also be considered in the geochemical modelling section (5.2) below.

5.1.2. *Main processes in the mid to lower crust: Holes GT2A and GT1A*

Most of the Samail ophiolite mid to lower crustal gabbros from Holes GT1A and GT2A are cumulate rocks and therefore expectedly have lower S concentrations than evolved MORBs from the EPR (1250 ± 200 ppm, Alt and Shanks, 2011). A significant number of studied samples have sulfide concentrations lower than depleted mantle values (120 ± 30 ppm, Salters and Stracke, 2004) (Fig. 11). Results from this study reveal that rocks with the lowest S concentrations are from fault damage zones where there was near complete leaching of magmatic sulfides without the deposition of secondary sulfides. Leaching, melting and equilibrium oxidation of magmatic sulfides will decrease total sulfide contents without imparting changes in isotopic values (Alt et al., 2007). All other mid-lower crustal gabbros with ($TS_{Sulfide}$ values between 120 and 1200 ppm) have sulfide sulfur concentrations within the range of in-situ gabbroic oceanic crust and Troodos lower gabbros. The least altered rocks (defined here as rocks less affected by post-magmatic processes with <50 % hydrothermal sulfide) have $TS_{sulfide}$ values that vary by one order of magnitude (114 and 1050 ppm) suggesting a wide range of primary sulfur concentrations in the cumulates due to segregation and mobility of sulfide melts within the cumulate mush.

Regardless of the intensity of hydrothermal and tectonic-induced alteration, both Holes from the Samail mid- to lower crustal section (Hole GT2A and GT1A) broadly preserve magmatic isotope signatures (Sakai et al., 1984). This is consistent with results obtained by SIMS showing that the entire spectrum of analyzed sulfides, from secondary (hydrothermal or metasomatic) to partly remobilized sulfides, chiefly retained their magmatic signatures. The sole exception are pyrrhotite laths within late-formed smectite aggregates replacing olivine, which have mildly negative sulfur isotope signatures, with $\delta^{34}S$ values as low as −5.0 ‰. Otherwise, the Samail lower crust is similar to most gabbroic sections of oceanic crust (Fig. 11) where a few ^{34}S-enriched samples in the uplifted crust of SWIR (ODP Hole 735B; Alford et al., 2011) have been attributed to closed system microbial sulfate reduction (MSR) that can lead to heavy signatures due to reservoir effects.

5.2. *Geochemical modelling of sulfur geochemistry processes*

Only one sample from Hole GT3A can be reasonably attributed to biogenic mediated processes. Consequently, in this section we focus on high-temperature abiogenic processes dominating sulfur cycling during hydrothermal alteration of the Samail ophiolite crust. Due to their greater sensitivity in assessing mass-dependent sulfur isotope fractionation, modelling will concentrate on the multiple sulfur isotope dataset, using mixing model formulations for thermochemical sulfate reduction (TSR) that take into account temperature (Section **5.2.2**) and variable sulfur concentrations (Section **5.2.3**) in the system.

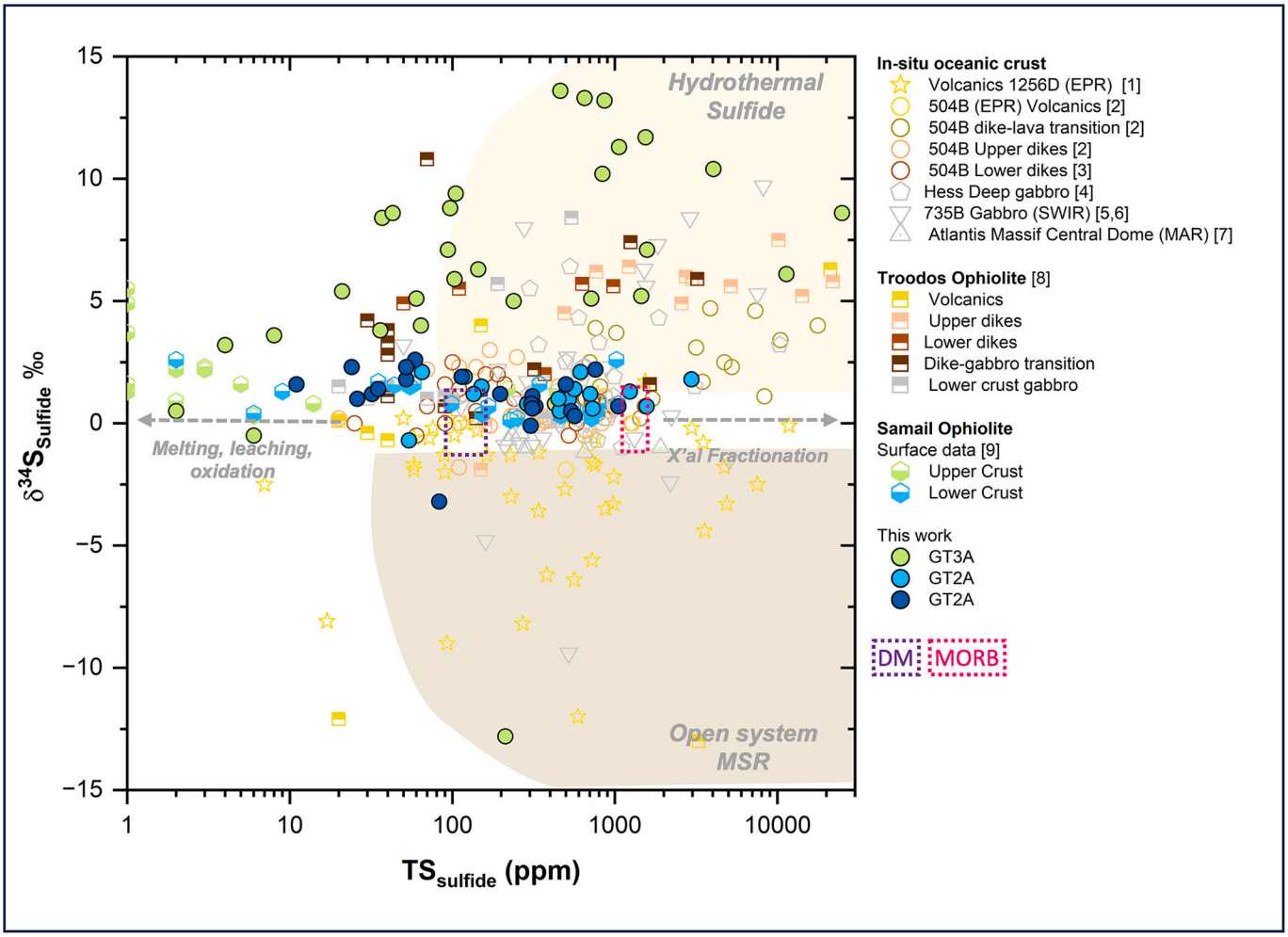

Fig. 11. Sulfur geochemistry showing sulfide sulfur ($TS_{Sulfide}$) versus $\delta^{34}S_{Sulfide}$. Arrows indicate processes that can lead to sulfur loss via melting, leaching or oxidation and sulfur increase via crystal fractionation without changes in the isotopic composition; the fields indicate expectable isotope compositions for sulfides formed via open system Microbial Sulfate Reduction (MSR) or Hydrothermal Sulfide Addition via Thermochemical Sulfate Reduction (TSR), based on Alt et al., 2007. Ocean crust data from: [1]- Alt and Shanks, 2011; [2]- Alt et al., 1989, [3]- Alt et al., 1995, [4]- Puchelt et al., 1996, [5] Alt and Anderson, 1991, [6] Alford et al., 2011, [7] Delacour et al., 2008a, [8] Alt, 1994, [9] Oeser et al. (2012). Also shown for reference: MORB $\delta^{34}S$ Sakai et al. (1984), sulfur contents for EPR glasses Alt et al. (2010), depleted mantle (DM) Salters and Stracke (2004).

5.2.1. Input isotope values for TSR mixing models

The main pools of sulfur involved in both low temperature and hydrothermal processes affecting the oceanic crust are magmatic sulfide and seawater sulfate. Recent measurements of quadruple sulfur isotopes on MORB samples suggest an average composition for the Depleted Mantle reservoir of $\delta^{34}S$ -1.28 ± 0.33 ‰ (Labidi et al., 2014) instead of the canonical value of 0.3 ± 0.5 ‰ of Sakai et al. (1984). Our whole rock measurements in mid-lower crustal samples with more than 70 % magmatic sulfides show values between −0.1 ‰ and + 1.9 ‰ with median close to +1 ‰. Although in-situ SIMS measurements show some anomalous pyrrhotite isotopic compositions (sample GT1A-152Z-3 0–8 cm), the positive sulfur isotope signatures in magmatic chalcopyrite and whole-rock data for fresh samples strongly suggest that the integrated monosulfide from which pyrrhotite-chalcopyrite-pentlandite were exsolved had a slightly positive signature. This would lie within the +0.3 ± 0.5 ‰ range suggested by Sakai et al. (1984) and therefore we use the value of 0 ‰ as a reference in our calculations.

Mantle isotope compositions for $\Delta^{33}S$ are 0 ‰ (Labidi et al., 2012; Ono et al., 2007). However, data from incipiently hydrothermally altered mid-lower crustal sections from this work and Oeser et al. (2012) are consistently negative. Indeed, irrespective of the model considered below, any set of curves calculated assuming mantle compositions of $\Delta^{33}S$ = 0 ‰ (Labidi et al., 2012; Ono et al., 2007) falls out of the compositional space of the samples studied (stippled curves in Fig. 12). Considering that Samail mid-lower crustal rocks preserving magmatic sulfides have isotope compositions as low as $\Delta^{33}S$ = -0.042 ‰, we used a value of −0.045 ‰ for the mantle composition in the models below (solid lines in Fig. 12), although the model curves for the canonical mantle value are also depicted (stippled lines) for comparison. The potential causes for the deviation of $\Delta^{33}S$ values relative to canonical values require further investigation. We propose a provisional explanation that relates to the Indian MORB geochemical features of the Samail mantle source (Godard et al., 2006; Jesus et al., 2022). Indian MORB presumably taps slab-derived components from old subduction zones where sediments with mass independent fractionation (MIF) signatures could provide the mild but systematically negative $\Delta^{33}S$ signatures to the Samail crust. Recycling of old sedimentary slab-derived components has been documented for example in the Mangaia plume considered to be an end-member for high-μ mantle where Archean sediments were recycled (Cabral et al., 2013).

Mesozoic seawater sulfate isotope composition was lower than modern day ($\delta^{34}S$ = 21.5 ± 0.5‰; Johnston et al., 2014), between +16 to +22 ‰ (Kampschulte and Strauss, 2004). During the Cretaceous, compositions were closer to +18 ‰ (Kampschulte and Strauss, 2004;

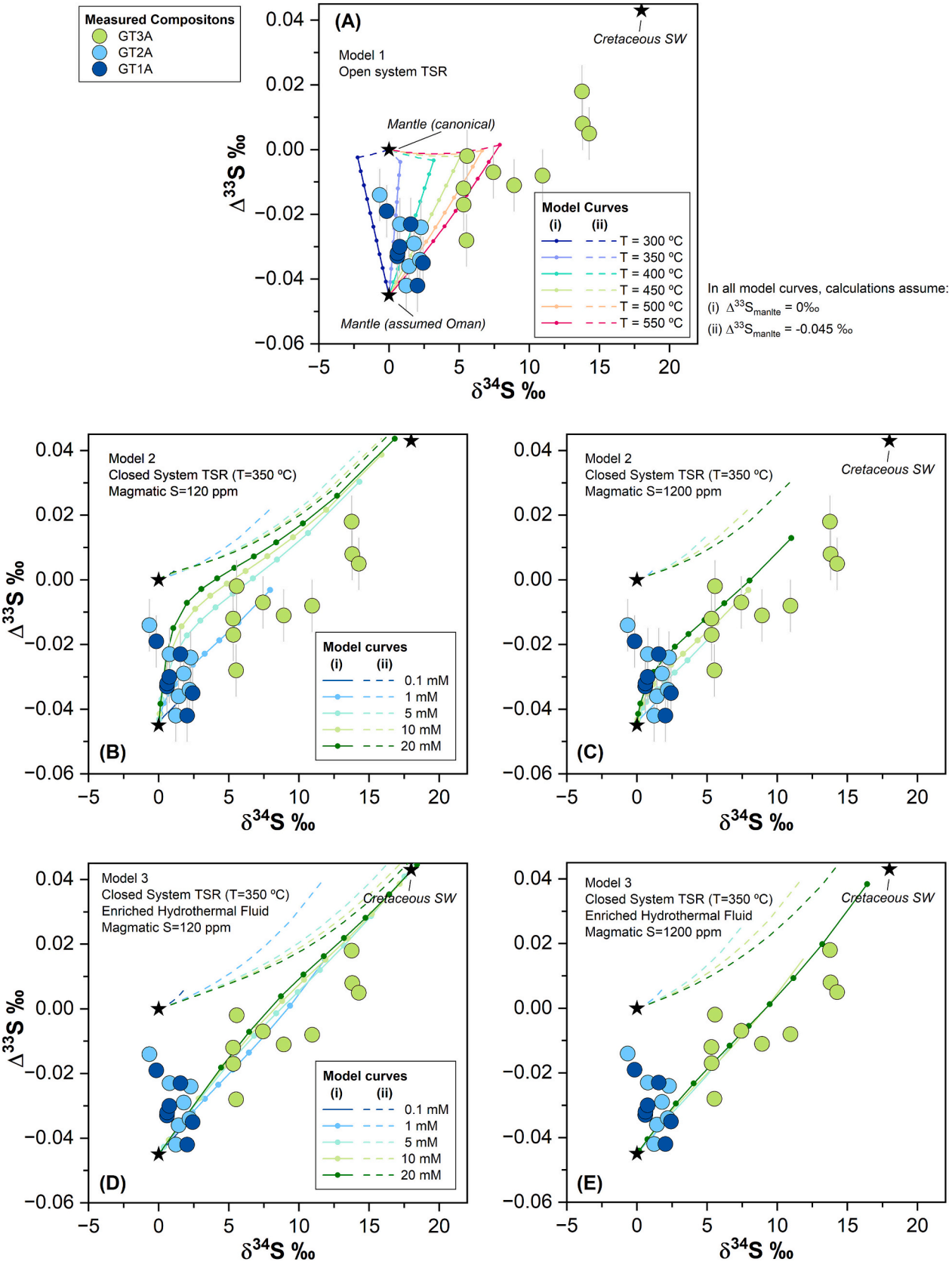

(caption on next page)

Fig. 12. Modelling of sulfide compositions using different mixing models for TSR. In all plots, curves represent the pooled (or accumulated) composition of H_2S: the upper set of stippled curves (ii) were calculated using the canonical mantle composition $\Delta^{33}S = 0.00$ ‰ and cannot explain the composition of OmanDP samples. Therefore the solid curves (i) were calculated using $\Delta^{33}S = -0.045$ ‰, as discussed in the text. Nodes in model curves represent increments of mixing from $f = 0.001$ to $f = 1$. Additional input parameters common to all models: magmatic sulfur $\delta^{34}S = 0$ ‰ (Sakai et al., 1984), Cretaceous seawater $\delta^{34}S = 18$ ‰ (Kampschulte and Strauss, 2004; Paytan et al., 2004) $\Delta^{33}S = 0.043$ ‰ (Masterson et al., 2016). **(A)** Model 1: Open system mixing for TSR at variable temperature [300–550] °C; **(B—C)** Model 2: Closed system, Rayleigh distillation for TSR assuming magmatic sulfur concentrations of 120 (B) and 1200 ppm (C), calculated for different sulfate concentrations in the hydrothermal fluid, corresponding to the coloured curves; **(D-E)** Model 3: Closed system, Rayleigh distillation for TSR assuming magmatic sulfur concentrations of 120 (D) and 1200 ppm (E), calculated for different sulfate concentrations in the hydrothermal fluid corresponding to the coloured curves in model 3; it is assumed that the hydrothermal fluid has undergone 40 % isotopic enrichment relative to Cretaceous seawater during closed system evolution within the hydrothermal system ($\delta^{34}S = 26.8$ ‰, $\Delta^{33}S = 0.091$ ‰; see Supplementary Material SM2 Fig. 2). Note that for models 1 and 2, assuming a magmatic S concentration of 1200 ppm results in a sulfide product with very little isotopic fractionation, therefore the resulting curves are very short and plot close to the mantle composition being hard to depict.

Paytan et al., 2004) and we use this value in our modelling together with $\Delta^{33}S$ of 0.043 ± 0.016 ‰ following Masterson et al. (2016).

In all mixing models presented below (Fig. 12), the plotted $\delta^{34}S$-$\Delta^{33}S$ curves represent the pooled (accumulated) product composition of H_2S for a given fraction of the mixture (*f*). Fractionation factors between sulfide and H_2S increase with decreasing temperature, being highest for pyrite at 300 °C ($\Delta_{Py\text{-}H2S} = 1.22$ ‰) Ohmoto et al., 1979. These values are one order of magnitude smaller than the isotope fractionations for seawater sulfate reduction to H_2S (10.1 to 20.2 ‰; see 5.2.2.) at the temperatures considered in modelling (550–300 °C). Therefore, we take the composition of H_2S in the models to be chiefly identical to the resulting hydrothermal sulfides since this will have a negligible bearing on the model sulfide compositions.

5.2.2. *Open system mixing model for TSR as a function of temperature*

Within the high-temperature zone at the base of the upper crustal hydrothermal system, the H_2S in the fluid will result from a mixture of (Ono et al., 2007; Shanks, 2001): a) magmatic H_2S leached from the magmatic sulfides in the basaltic (s.l.) rocks (Woodruff and Shanks III, 1988) and; b) thermochemically reduced sulfate in the presence of ferrous-bearing minerals (Shanks et al., 1981). Mixing model 1 in Fig. 12A shows the effects of open-system thermochemical sulfate reduction (TSR) under a range of temperatures between 300 and 550 °C appropriate for high-temperature seafloor hydrothermal systems (Shanks, 2001). Fractionation factors for SO_4-H_2S are temperature dependent and were calculated for $^{34}\alpha$ from Ohmoto and Lasaga (1982), where T is temperature in Kelvin (Eq. (4)):

$$ln^{34}\boldsymbol{\alpha} = \frac{\mathbf{6.463 \times 10^6}}{\boldsymbol{T^2} + \mathbf{0.56}} \quad (4)$$

For mass-dependent SO_4-H_2S ^{33}S fractionation processes, the temperature dependence of the fractionation factor $^{33}\alpha$ can be related by the empirical expression for $^{33}\theta$ (Ono et al., 2007; Eq. (5)) which at high temperatures approaches the value 0.515 in Eq. (2).

(5)

For each temperature, the sulfide produced from seawater TSR is mixed with the mantle isotope composition following a simple binary mixing model (Eq. (6)) where *x* refers to ^{33}S, ^{34}S.

$$\boldsymbol{\delta^x_{Mixture}} = \mathbf{f} \times \boldsymbol{\delta^x_{Seawater}} + (\mathbf{1} - \mathbf{f}) \times \boldsymbol{\delta^x_{Magmatic}} \quad (6)$$

Even if only a negligible contribution of leached magmatic sulfide is assumed, in a seawater-derived sulfur dominated system, open-system TSR is only able to produce a relatively narrow compositional range. Fractionation factors increase with decreasing temperature ($T = 500$ to 300 °C, $^{34}\alpha \sim +20$ to +10‰), meaning that TSR will produce S with mildly positive values at 550 °C but slightly negative $\delta^{34}S$ compositions at low temperatures (Fig. 12A**)**. The Hole GT3A dike-gabbro transition zone samples mostly fall outside these model curves, with the high isotopic values implying that either a modified fluid, with S-isotopic compositions higher than Cretaceous seawater, was involved and/or there are reservoir effects that the open-system mixing models do not consider.

Lower crustal gabbro samples plot within a poorly defined region of the model, albeit following a trend that approaches the slope of lower temperature model curves. The formation of smectite-chlorite pyrrhotite aggregates should have occurred at temperatures below 200 °C (Alt et al., 2010). TSR is sluggish below 250 °C (Shanks et al., 1981) and the large fractionation factors at these temperatures ($^{34}\alpha = 24.2$ ‰) could produce sulfide with $\delta^{34}S$ values as low as −6 ‰. It is therefore possible that the formation of secondary pyrrhotite sulfide assemblages began close to the limiting temperatures for TSR with further alteration to smectite-chlorite stratified formation occurring at lower temperatures (<100 °C, Alt et al., 2010).

5.2.3. *Closed-system mixing model for TSR as a function of S concentrations*

The amount of sulfur available in the different reservoirs, namely the proportions of S from magmatic rocks and sulfate in the seawater-modified hydrothermal fluids, provide additional constrains on sulfur isotope variations. Mixing models 2 and 3 in Fig. 12B-D take into account reservoir effects arising from closed system evolution of the hydrothermal system for different seawater and magmatic sulfur concentrations, following Rayleigh fractionation formulations adapted by Schwarzenbach et al. (2018). Based on MgO-S relationships for the dikes and frozen melts of the axial melt lens (Eq. (3)), primary sulfur concentrations in the upper crustal section are estimated between ~850 and ~ 1700 ppm. The application of Eq. (3) to the mid-lower crustal rocks is precluded because these are cumulates and do not represent melts. Based on median and maximum $T_{Sulfide}$ extracts (Table 1 and Fig. 8), a wide permissible range of S concentrations is indicated: $X =$ 454 ppm, max = 2951 ppm for mid-crustal GT2A cumulates and $X =$ 114 ppm, max = 1050 ppm for GT1A lower crustal cumulates. To accommodate for this wide range, models consider initial magmatic sulfur concentrations of 120 and 1200 ppm. Temperature was fixed at 350 °C which is representative of the base of an upper crustal hydrothermal system reaction zone near the dike-gabbro transition (Alt, 1995; Hannington, 2014) and would also overlap with dominant conditions in the mid-lower crustal section. Similar to S isotope compositions, seawater sulfate concentrations in the Mesozoic were lower than modern-day seawater, with the best estimates being 2–12 mM (Timofeeff et al., 2006). However, anhydrite displays retrograde solubility and upon reaching ~150 °C anhydrite should precipitate from seawater-derived fluids that will significantly deplete the sulfate concentrations of recharge fluids, meaning a much smaller amount of sulfate will reach the deeper parts of the hydrothermal system (Seyfried Jr and Bischoff, 1981; Sleep, 1991; Teagle et al., 1998). Accordingly, our models consider a range of sulfate concentrations in the fluid from the experimental minimum of 0.1 mM (Seyfried Jr and Bischoff, 1981) to 20 mM, which is above the 12 mM limit proposed for the Cretaceous (Timofeeff et al., 2006).

Mixing model 2 (Fig. 12B-C) shows the sulfide composition that forms from fluids with a starting isotopic composition equal to

Cretaceous seawater at variable sulfate concentrations, represented by the various coloured lines. For high concentrations of magmatic sulfur (1200 ppm), the resulting hydrothermal sulfide is buffered by the mantle isotopic composition, only reaching $\delta^{34}S > 5$ ‰ at high sulfate concentrations in the fluid (>10 mM). Nevertheless, the heaviest isotopic composition that can be produced under these model conditions (+11 ‰) is insufficient to explain many of the heavier samples from the Hole GT3A dike-gabbro transition zone. For magmatic sulfur concentrations of 120 ppm, the model sulfide compositions are closer to those measured in Hole GT3A if sulfate concentrations in the fluid are ≥ 5 mM, although

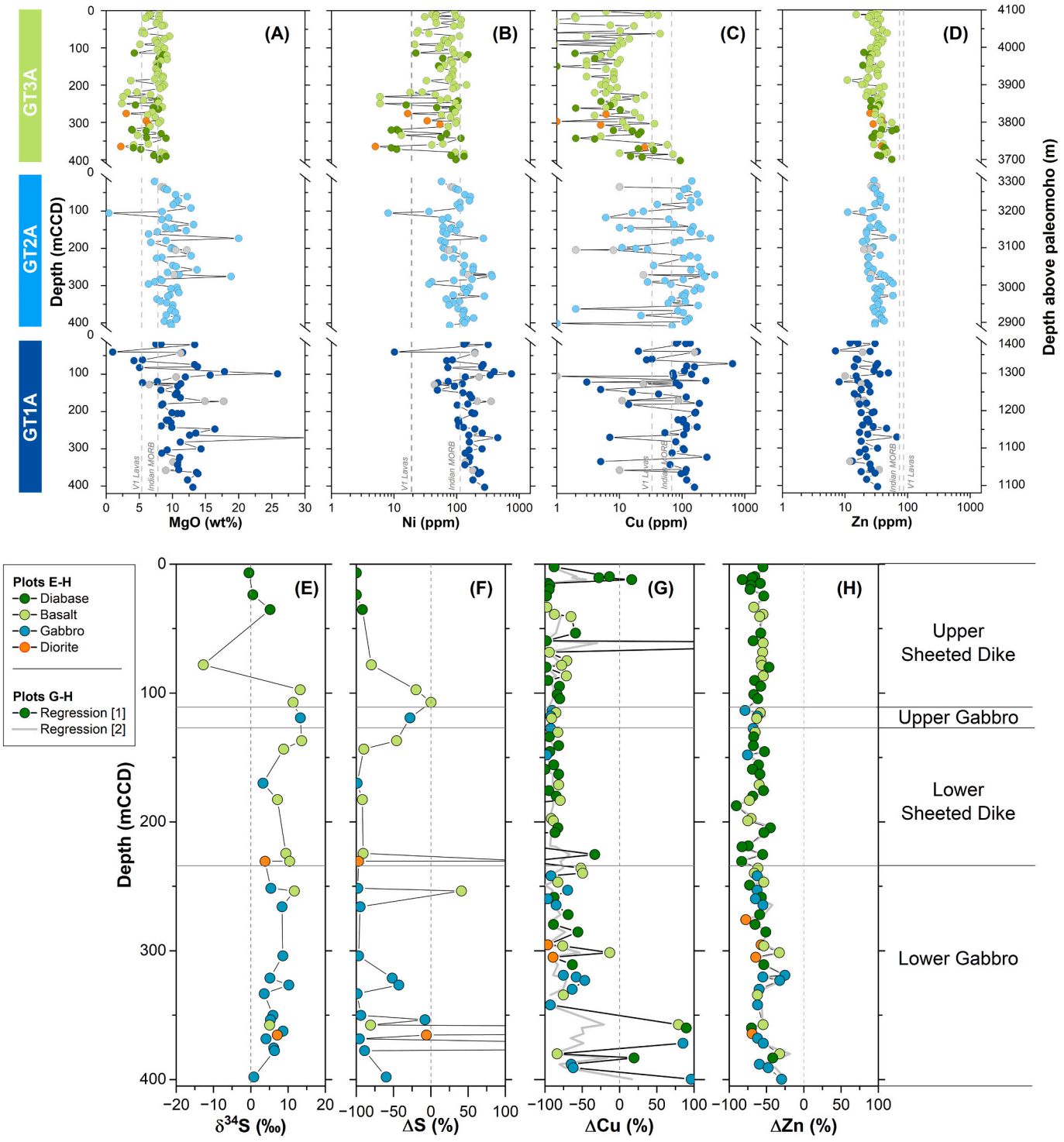

Fig. 13. (A-D) Cu, Zn, Ni and MgO concentrations for OmanDP Gabbro-Transect drillholes using OmanDP shipboard analyses (Kelemen et al., 2020). Reference values: Geotimes V1 lavas (Belgrano et al., 2019; Indian MORB (White and Klein, 2014). **(E-H)** Sulfur and base metal mass balance for the upper crustal section GT3A showing the $\delta^{34}S$ Isotope values (E) for comparison; consult section 2.2.1 for details on GT3A lithostratigraphy. (F) Mass balance for sulfur based on data obtained in this work. (G-H) Mass balance for base metals using OmanDP shipboard data from Kelemen et al., 2020 wherein two regressions lines are shown: [1] black line with symbols is based on Geotimes lavas (Belgrano et al., 2019) and [2] grey line (symbols are omitted for clarity) is based on regressions using EPR basalts compiled by Gale et al. (2013), for further details consult SM3.

the corresponding $\Delta^{33}S$ values are higher than our samples.

Mixing model 3 (Fig. 12D-E) introduces the effects of a hydrothermal fluid with isotopic composition heavier than that of Cretaceous seawater, based on the residual fluid from model 2 (for details see Supplementary Material SM2, Fig. 2). The best fit was obtained for a fluid that has undergone 40 % isotopic enrichment ($f = 0.6$) relative to Cretaceous seawater during closed system evolution within the hydrothermal system ($\delta^{34}S = 26.8$ ‰, $\Delta^{33}S = 0.091$ ‰). This model shows a good fit to measured results, accounting for the heavier isotope compositions recorded in Hole GT3A, even for an initial magmatic S concentration of 1200 ppm (closer to the estimates for our samples). Furthermore, there is a good adjustment for scenarios with low initial sulfate concentrations in the hydrothermal fluid which are likely more realistic with those reaching the roots of the hydrothermal system (Seyfried Jr and Bischoff, 1981; Sleep, 1991; Teagle et al., 1998).

Models 2 and 3 do not provide additional constrains for sulfide formation in mid-lower crustal rocks. At lower temperatures all curves would follow to a trend towards lower $\delta^{34}S$ values at increasing $\Delta^{33}S$ values as seen in Model 1 (Supplementary Material SM2, Fig. 2). Given the significantly lower degree of alteration in most mid-low crustal rocks, it is reasonable that most high temperature alteration proceeded under low fluid/rock ratios and closed system conditions which cannot be resolved by the models. Mid-lower crustal samples that experienced stronger degrees of alteration under sub-greenschist conditions, such as faulted intervals or the pyrrhotite-smectite aggregates in non-faulted rocks, the lower temperature trend in Model 1 remains the best approach.

5.3. Sulfur and base metal mobility during hydrothermal alteration

Fig. 13 A-D shows selected base metal and MgO concentrations in the crustal section from shipboard data (Kelemen et al., 2020) plus reference values for Indian MORB (White and Klein, 2014) and the axial Geotimes volcanic unit, contemporaneous to the crustal accretion stage (Belgrano et al., 2019). As evidenced by MgO and Ni concentrations, Geotimes lavas are more differentiated than Indian MORB (e.g. Godard et al., 2006) with samples from Hole GT3A straddling between both. The mid-lower crustal gabbros (GT1A and GT2A) show a gradual increase in MgO and Ni downhole due to the combined effects from increasing primitive character of the melts and olivine accumulation. Mg—Ni troughs correspond to anorthosite, and peaks to ultramafic layers. Zn concentrations increase stepwise from the layered (Hole GT1A) to the foliated gabbros (Hole GT2A), following an expectable differentiation trend, but Hole GT3A dike and gabbros concentrations are below the range for the Geotimes lavas. The high Cu concentrations in the mid-lower crustal section are consistent with early sulfide saturation and the common occurrence of chalcopyrite in magmatic and hydrothermal sulfide assemblages. Contrarily to what is observed for Ni or Zn, strongly altered rocks in the lower crust have vanishingly low Cu concentrations. The dike-gabbro transition section shows a remarkable Cu distribution, with concentrations close to MORB at the bottom smoothly decreasing to a minimum at ca. 200 m (< 10 ppm), then slowly increasing towards the top of Hole GT3A. A more subtle similar trend can be observed for Zn. The behavior of Cu and to a lesser extent Zn, in the upper crust suggest moderate to extensive metal mobilization during hydrothermal alteration. The depletion of Cu in altered rocks of the mid-lower crustal section is consistent with similar, but localized processes, that did not affect Zn or Ni to the same extent. Ni and Zn occur in magmatic sulfides, but also in silicates and oxides. Where alteration did not lead to the formation of secondary sulfides, as in mid-lower crust most altered domains, once the primary phase is destroyed, Ni and Zn can be re-incorporated in secondary silicate (serpentine, amphibole) or magnetite, whereas Cu will be transported out of the system.

5.3.1. A semi-quantitative assessment of Cu, Zn and S mobility in GT3A Hole

An accurate quantification of metal mobilization requires knowledge of chalcophile and immobile elements in fresh glasses which are currently unavailable for Oman (Jowitt et al., 2012; Patten et al., 2016). We provide a semi-quantitative assessment of Cu, Zn and S mobilization in the upper crust frozen melts where metal mobilization was widespread and magmatic accumulation is less likely to modify primary magmatic concentrations. Estimated magmatic Cu and Zn concentrations were calculated for each sample from the shipboard dataset based on the regression of metal concentrations relative to Y measured in Geotimes samples by Belgrano et al. (2019). Because Geotimes lavas are spilitised and may have experienced base metal mobilization, magmatic values were also computed for EPR basalts compiled by Gale et al. (2013) for comparison. Results for baseline magmatic concentrations are quite similar for Zn but lower Cu concentrations are estimated based on Geotimes lavas (details can be found in Supplementary Materials SM3, Fig. 2).

Sulfur measurements are unavailable for Oman shipboard samples, therefore we rely on MgO-S relationships from Alt and Shanks (2011) (Eq. (3)) only for samples studied in this work. Although MgO is mobile during seawater-rock reactions, net fluxes estimated for the oceanic crust dike section are mainly zero (Staudigel, 2014). Crucially, Hole GT3A alteration is dominated by albitization and amphibolitization rather than chlorite formation. Hydrothermal amphiboles most commonly record the Mg# of the primary pyroxenes (Gillis, 1995), unlike chlorite which can effectively accommodate seawater Mg, but is largely subordinate to amphibole in Hole GT3A.

The final mass balance for Cu, Zn and S is given by **Eq. (7)** where E^i_{sample} and $E^i_{magmatic}$ are the concentrations of the element measured in the altered sample and estimated for the magmatic protolith, whereas ΔE^i is the mass variation for that element (Jowitt et al., 2012).

$$\mathbf{\Delta E^i} = \frac{\mathbf{E^i_{sample} - E^i_{magmatic}}}{\mathbf{E^i_{magmatic}}} \mathbf{*100} \quad (7)$$

Mass balance for sulfur was made for all samples studied in this work and results are shown in **Fig. 13E-F** alongside with the isotope values for comparison. **Fig. 13G-H** shows the results for Cu and Zn mass balance using all shipboard samples: the black and grey data series refer to estimates based on a magmatic baseline that considers Geotimes and EPR basalts magmatic concentrations, respectively. Details of the regressions are provided in **SM3** and summary statistics are listed in Table 4A. Results based on Geotimes versus those obtained with EPR lavas are identical for Zn but differ for Cu. Due to the higher magmatic baseline concentrations for EPR lavas, these estimates indicate more extreme Cu losses, namely in sections where the Geotimes-based estimates would suggest moderate Cu-gains (**Fig. 13G**). Because currently there are no means to assess how much the Cu magmatic concentrations in Geotimes lavas might have been lost during spilitization, we will consider these semi-quantitative results in the forthcoming discussion, as they provide a more conservative estimate of Cu losses compared to those provided by the EPR baseline.

Indeed, regardless of the regression considered, results suggest that most of the studied upper crustal section experienced extensive (>80 %) to near complete leaching of the magmatic sulfur content. Sulfur gains due to hydrothermal sulfide deposition are restricted to the Hole GT3A Lower Gabbro Sequence. Rocks that experienced >80 % sulfur loss have enriched $\delta^{34}S$ values of up to +10 ‰, whereas those with heaviest isotopic composition have sulfur losses up to ~60 %.

ΔE^{Zn} estimates are relatively constant, without intervals of major Zn enrichment, as expected considering the absence of sphalerite and low Zn contents in other sulfide phases. Results confirm that the uppermost ~12 m of Hole GT3A show the most significant Zn losses ($X\Delta E^{Zn} = -68$, $\sigma = 11$), compared to Cu ($X\Delta E^{Cu} = -22$, $\sigma = 43$). Below this interval, down to ~342 m, Cu losses are extensive to near complete ($X\Delta E^{Cu} =$

Table 4
(A) Summary statistics for mass balance of S (using measurements on samples from this work), Cu and Zn (using all shipboard samples) in Hole GT3A (see text for details). **(B)** Estimated mass of sulfur and metals released during hydrothermal alteration of GT3A rocks using section length weighted average of results from table A. Samples recording S or metal gains were excluded, it is assumed the corresponding mobilised mass was redistributed within the crust. Densities for each sequence from shipboard data (Kelemen et al., 2020).

	Based on Geotimes Lavas [B]						Based on EPR basalts [C]			
(A)	S magmatic (ppm)	Δ S (%)	Cu magmatic (ppm)	Δ Cu (%)	Zn magmatic (ppm)	Δ Zn (%)	Cu magmatic (ppm)	Δ Cu (%)	Zn magmatic (ppm)	Δ Zn (%)
Median	1285	−85	47	−83	79	−61	80	−89	74	−58
Average	1298	21	45	−61	85	−61	76	−83	83	−58
Min	851	−100	8	−100	67	−91	42	−100	52	−92
Max	1716	1684	69	427	134	−25	89	17	166	−19
Standard Dev	259	342	13	72	14	12	10	21	24	14
n samples	30	30	83	83	83	83	83	83	83	83

(B)			Length- weighed average mobilised mass (ppm)			Length- weighed average mobilised mass (Kg/m^3)		
	Length (m)	Grain density (g/cm^3)	S	Cu	Zn	S	Cu	Zn
Upper dyke	111.0	2.91	806	40	49	2.3454	0.1164	0.1413
Upper Gabbro	16.9	2.87	280	48	59	0.8028	0.1376	0.1692
Lower dyke	106.0	2.88	1027	43	64	2.9592	0.1249	0.1843
Lower Gabbro	166.2	2.91	1149	30	45	3.3450	0.0873	0.1307
GT3A BULK		**2.88**				**2.8394**	**0.1065**	**0.1483**

−85, σ = 66) and show no correlation with sulfur mass variations or isotope signatures, as exemplified by intervals with higher sulfidation comprising isotopically heavy pyrite. These features suggest that between 12 and 342 m Cu was substantially leached out of the system. The lowermost portion of the hole (below 347 m) is characterized by smaller Cu losses or modest gains due to the greater presence of chalcopyrite.

5.4. Implications for fluid circulation in the oceanic crust

5.4.1. The origin of sulfates in the lower crust

Three samples yielded high sulfate fraction extracts (TS_{SO4}/TS_{ext} 0.41 to 0.96) with a sulfur isotopic composition close to that of Cretaceous seawater, +16.1 ‰ to +17.3 ‰ (Fig. 9B). These samples are associated with intervals of intense deformation representative of extensively metasomatized gabbro. As noted above, these deformed rocks show the effects of extensive magmatic sulfide leaching without hydrothermal sulfide precipitation, apart from traces of pyrite. Some of these intervals likely correspond to fault infills of the Zihlmann-Müller fault zone (ZMFZ, Kelemen et al., 2020; Zihlmann et al., 2018) intersected in Hole GT1A. As is common in other ocean-crust studies (e.g. Alt and Anderson, 1991) no sulfates were observed petrographically or imaged using compositional EDS scans in our wall rock samples (this study). However, thick anhydrite veins (>10 cm) are associated with brittle structures in Holes GT1A and GT2A (Kelemen et al., 2020; Teagle et al., 2019), and therefore it is reasonable that (sub-) microscopic veinlets are present throughout the fault damage zones.

The presence of sulfates in deep seated oceanic faults documents the inflow of seawater that precipitated anhydrite upon reaching temperatures of ~150 °C (Kleine et al., 2022; Seyfried Jr and Bischoff, 1981; Sleep, 1991; Teagle et al., 1998; Teagle et al., 2019). Anhydrite veins were documented in the Atlantis Massif (Delacour et al., 2008a) to a depth of 700 m in Hole U1309D whereas Hole GT1A represents a paleodepth >5 km below the seafloor implying deep-seated hydrothermal recharge. Due to anhydrite's retrograde solubility, it is commonly assumed that it dissolves back into the oceans during off-axis circulation within the upper crust (e.g., Alt, 1995; Kleine et al., 2022). The precipitation and preservation of anhydrite in Holes GT1A and GT2A requires that the lower crust remained at $T > 150$ °C until the system was effectively closed to seawater interaction. This could occur when high temperature, upwelling hydrothermal circulation (e.g., as documented in the ZMFZ by Zihlmann et al., 2018) wanned and downwelling fluids enabled anhydrite precipitation or, spatially close recharge-discharge during the axial stage. Crucially, the occurrence of Cretaceous seawater sulfate in several fault-zones logged in Holes GT1A and GT2A, attests to the complexity, and likely longevity, of the plumbing system of deep-seated oceanic fault zones.

Other sulfates identified in the mid-lower crustal section represent a residual amount of the extracted sulfur fraction in that sample (TS_{SO4}/TS_{ext} 0.01 to 0.09) and display isotopic compositions slightly higher ($\delta^{34}S_{SO4}$ + 2.8 ‰ to +5.7 ‰) than the coexisting sulfides ($\delta^{34}S_{Sulfide}$ + 0.8 ‰ to +1.2 ‰) resulting in $\Delta_{SO4\text{-}Sulfide}$ between +1.8 ‰ and + 5.1 ‰. Abiotic oxidation of sulfide to sulfate under acidic conditions (pH < 3) produces negligible $\Delta_{SO4\text{-}Sulfide}$ (Taylor et al., 1984) whereas under neutral to alkaline conditions (pH 8–11), $\Delta_{SO4\text{-}Sulfide}$ are −5.2 ± 1.4 (Fry et al., 1988). Only one sulfate sample from Hole GT3A has negative $\Delta_{SO4\text{-}Sulfide}$ of −1.2 ‰. The strong base metal leaching within Hole GT3A requires acidic, black smoker-like fluids (Seyfried Jr and Bischoff, 1981), therefore this small negative $\Delta_{SO4\text{-}Sulfide}$ could reflect sulfide oxidation during the off-axis stage, under the influence of neutral to slightly alkaline seawater. The lower crustal sulfates showing larger positive $\Delta_{SO4\text{-}Sulfide}$ imply that sulfide oxidation occurred under acidic conditions, likely under the influence of residual hydrothermal fluids at temperatures between ~250–150 °C when TSR was no longer possible.,

5.4.2. Constrains to hydrothermal circulation in the mid-lower oceanic crust

The secondary sulfide assemblage within mid-lower crust rocks comprises millerite + siegenite-polydimite$_{ss}$ + pyrite that formed by replacement of magmatic pyrrhotite-pentlandite in reactions such as Eq. (8) or Eq. (9). Chalcopyrite remained stable from the magmatic to hydrothermal stage, although dissolution-reprecipitation cannot be excluded based on its occurrence in veins (Fig. 4H). Millerite and polydymite upper temperature stabilities are bounded at 379 and 356 °C, respectively (Fleet, 2006), and their formation requires sulfur input to the system, enabling also the formation of pyrite.

$$FeS\ (Po) + (Fe_5Ni_4)S_8\ (Pn) + 7S = 4NiS\ (Mil) + 6FeS_2\ (Py) \quad (8)$$

$$FeS\ (Po) + 3\ (Fe_5Ni_4)S_8\ (Pn) + 23S = 4Ni_3S_4\ (Poly) + 16FeS_2\ (Py) \quad (9)$$

The formation of millerite implies slightly lower sulfur fugacity relative to polydymite-siegentite$_{ss}$ and indicates higher sulfidation conditions in the foliated (Hole GT2A) relative to the layered (Hole

GT1A) gabbros, where millerite is comparatively more abundant (Fig. 5). These mineralogical constraints are consistent with results from isotope modelling that suggest the studied mid-lower crustal rocks experienced small additions of seawater-derived sulfur via TSR down to ~300 °C (Fig. 12A). For a closed system evolution, the isotopic signature of the most isotopically modified rock ($\Delta^{33}S$ = -0.014 ‰) requires ~10 % input of seawater derived sulfur (Fig. 12B-C). In-situ isotope measurements show that metasomatic and hydrothermal sulfides express this progressive isotopic enrichment relative to magmatic and remobilized sulfide assemblages.

The observations for Hole GT1A and GT2A can be reconciled with the models for lower crustal cooling, albeit with fundamentally different outcomes on sulfur and metal cycling (Fig. 14). Away from intervals affected by fault zones, sulfide and silicate alteration is not pervasive with many sections preserving intact magmatic sulfide assemblages that also persist as remobilized remnants along with the hydrothermal sulfides. In these rocks, textural relationships indicate that the microvein network (Bosch et al., 2004; Manning et al., 2000) played a crucial role in sulfur and metal remobilization (Fig. 4D). The minor isotopic resetting suggests these rocks experienced redistribution of magmatic sulfur mixed with very small inputs of seawater-derived sulfur. As implied by mineral paragenesis, this evolution took place under very low fluid/rock ratios, moderate sulfur fugacities and essentially preserved base metal abundances as metasomatic and hydrothermal sulfides. Strongly altered domains such as the ZMFZ (Zihlmann et al., 2018) and the many faulted intervals present in Holes GT1A and GT2A, preserve lower temperature, sub-greenschist mineral assemblages and the effects of near-complete sulfur and metal mobilization. Such structures are the expression of crustal scale channeled hydrothermal fluid flow (Coogan et al., 2006) and the occurrence of sulfate with a Cretaceous seawater sulfate sulfur isotope signature (Fig. 9; Kelemen et al., 2020, Teagle et al., 2019) attests to their open-system behavior, representing a previously unaccounted sulfur budget introduced in the deep crust.

5.4.3. *The dike-gabbro transition and the roots of VMS systems*

The upper crustal dike-gabbro transition zone sampled by Hole GT3A experienced near-complete metamorphic recrystallization giving rise to a low variance, higher fS_2 sulfide assemblage (pyrite-chalcopyrite-bornite). Geochemical modelling of isotopic compositions implies ~20 to 80 % incorporation of seawater derived sulfur (Fig. 12B-E). To achieve the heavier sulfur isotope compositions (+10 to +14 ‰) it is necessary to invoke a fluid that experienced isotope enrichment relative to seawater due to closed-system reservoir effects, likely reflecting limited supply of sulfur into the system. Mass balance indicates extensive S and Cu losses that were either re-precipitated at higher (not drilled) crustal levels or vented to the seafloor.

The Hole GT3A matrix-forming mineral assemblages formed at low fluid/rock ratios (Kelemen et al., 2020) with the leaching of Cu in most of the Hole (between 12 and 342 m) requiring temperatures of 350 to 400 °C (Seyfried Jr and Bischoff, 1981) to solubilize Cu into the hydrothermal fluids. The smaller losses/localized Cu enrichment in the lowermost portion of Hole GT3A (below 347 m) are due to the formation of hydrothermal chalcopyrite rather than the preservation of magmatic sulfides. These changes suggest that the hydrothermal fluid may have had decreased capacity to transport Cu. The Fe/Cu ratio of VMS hydrothermal fluids increases mildly with decreasing pH or increasing chlorine in solution, but is mostly dependent on fO_2 (Seyfried Jr. et al., 1997). The major changes in the Hole GT3A mineralogy at depth reflect the increase in epidote due to increasing aCa^{2+}/aH^{+} (Kelemen et al., 2020) and magnetite in the oxide gabbros which could buffer the fluids at higher Fe/Cu and lower fO_2, favoring chalcopyrite precipitation. SIMS measurements show that chalcopyrite has slightly heavier isotope composition relative to coexisting pyrite and is therefore in isotopic disequilibrium regarding fractionations to H_2S (Ohmoto et al., 1979) or, formed from different fluids/stages. Gradual shifting to lighter isotope compositions towards the bottom of the Lower Gabbros, along with the less pronounced sulfur losses in this unit, suggests a sulfate-depleted fluid at this depth. Excluding later effects from late MSR processes, the rocks in the uppermost section of Hole GT3A (above ~90 m) have $\delta^{34}S$ values of +5 ‰ to 0 ‰. These domains were less affected by sulfur and Cu mobilization and did not experience hydrothermal sulfide deposition, despite displaying similar silicate alteration assemblages.

The lithology-weighted average of isotope compositions for Hole GT3A provides a $\delta^{34}S$ value of +5.8 ‰. This overlaps with the upper

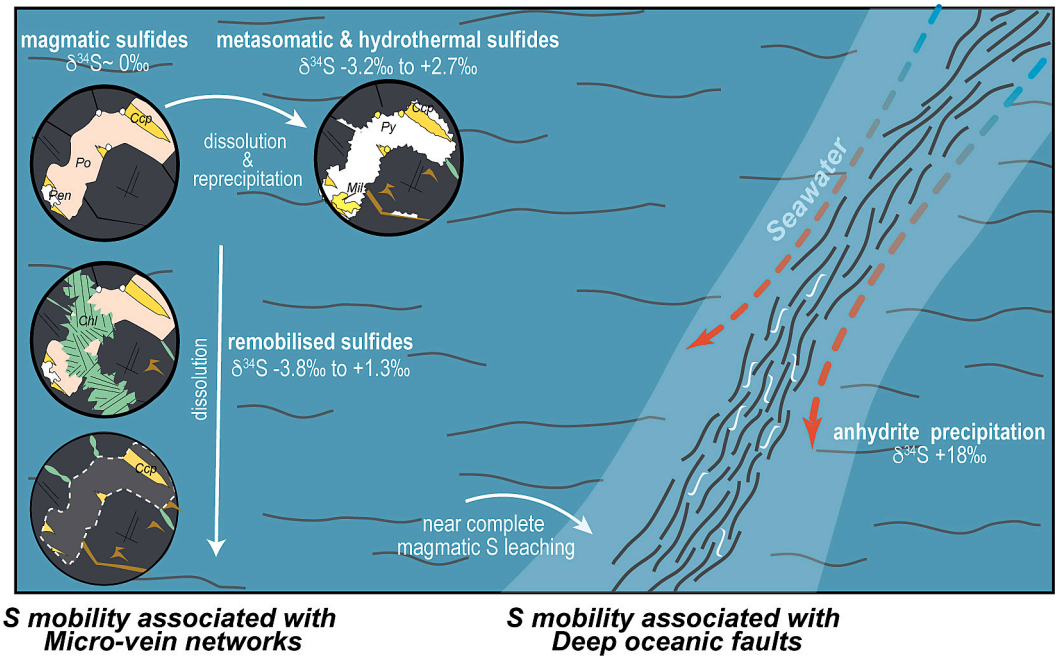

Fig. 14. Schematic evolution of sulfur cycling during magmatic and hydrothermal processes in the lower crustal gabbros (Holes GT1A and GT2A). Mineral abbreviations as in Fig. 4, brown and green veins or patches denote amphibole and chlorite infilling vein networks, respectively. (For interpretation of the references to colour in this figure legend, the reader is referred to the web version of this article.)

range of currently documented VMS deposits in Oman: their $\delta^{34}S$ values between −1.1 and + 5.4 ‰ are typical of unsedimented ridges (Jesus et al., 2022). Hole GT3A records significant sulfur isotope variability, with unusually heavy compositions relative to in-situ and ophiolitic oceanic crust (Fig. 11 and references therein). The dynamic magmatic-hydrothermal evolution proposed for the dike-gabbro transition (Engelhardt et al., 2022; France et al., 2021) and age relationships recorded in Hole GT3A may elucidate on the causes for such variations (Fig. 15).

(i) The hydrothermal system was initially perched above the axial melt lens (AML) represented by the Lower Gabbro, leaching the rocks of the Lower Dike Sequence that now record $\delta^{34}S$ values ~ + 10 ‰. (Fig. 15A).

(ii) Once the Lower Gabbro consolidated, the hydrothermal cells could penetrate, progressing downward into the AML (e.g. Gillis, 1995) and gradually forming isotopically lighter sulfides. Less comprehensive leaching of S and Cu also lead to increasing abundance in chalcopyrite. (Fig. 15B).

(iii) Relative ages based on cross-cutting relationships for Hole GT3A decrease upwards, suggesting that the Upper Gabbro Sequence was emplaced (slightly?) later, which could have triggered a renewed period of hydrothermal activity. Although the three dimensional geometry of the Upper Gabbro precludes precise assumptions, the localized isotopic enrichments within ±10 m of this Unit (Fig. **13**) and increasing $\delta^{34}S$ towards pyrite grain borders (Fig. 3A), are consistent with efficient focalizing of an isotopically heavy, rapidly evolving fluid (Fig. 15B). The origin of the isotopically enriched fluid (supported by our geochemical modelling) could lie on recycling of mature hydrothermal fluids from previous/on-going hydrothermal activity beneath.

(iv) The transition to isotope compositions closer to MORB in the remainder ~90 m of the Upper Sheeted Dike suggests a fluid buffered by magmatic sulfur, outside of the influence of the underlying Upper Gabbro. Although these values are closer to the compositional range of Oman VMS deposits or the sheeted dike section in Troodos (Alt, 1994) the relatively abrupt transition from fundamentally different isotopic domains and the unknown features of the thick crustal section above, advise caution in

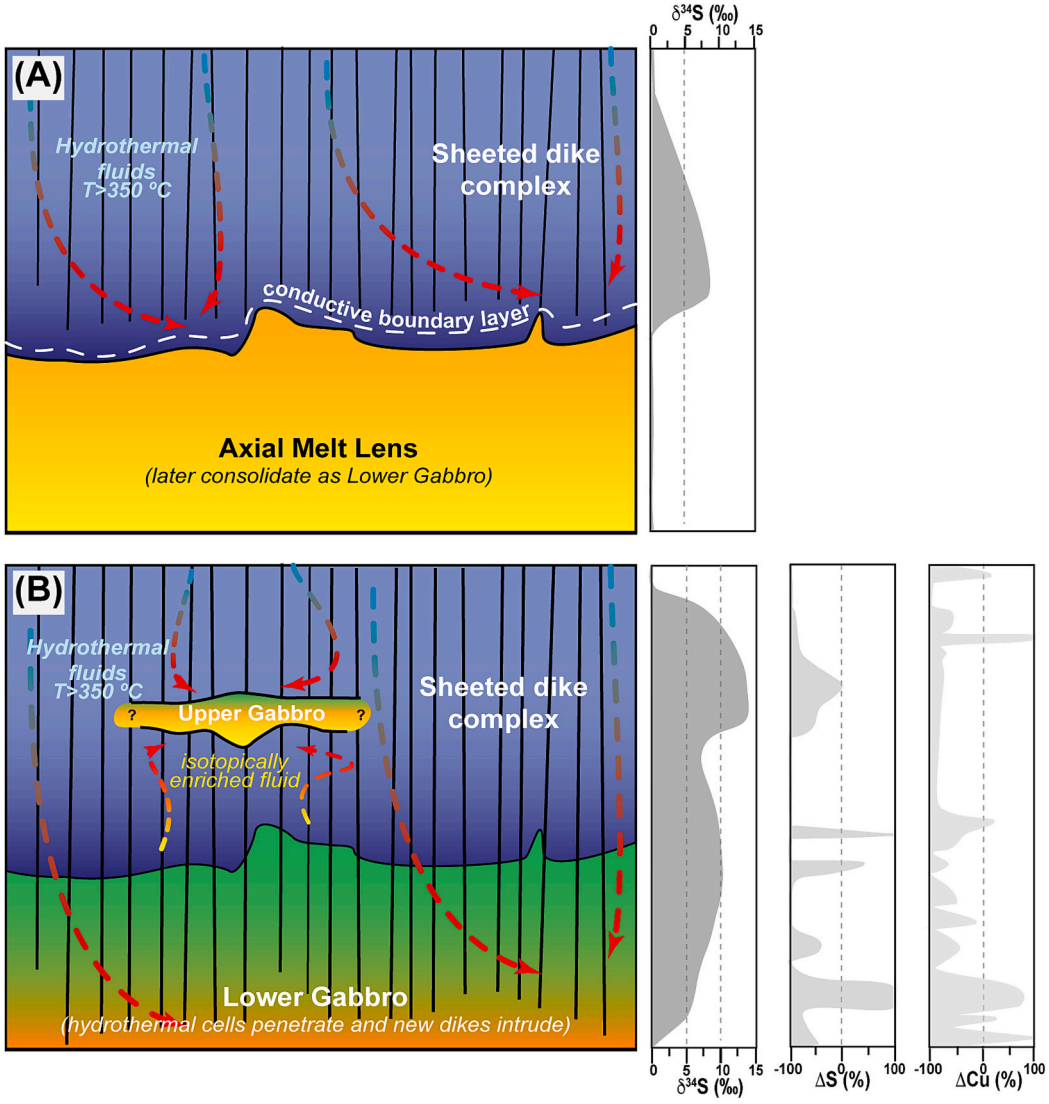

Fig. 15. Schematic evolution of sulfur cycling during magmatic and hydrothermal processes in the dike-gabbro transition (Hole GT3A). **(A)** Initial stage where the Lower Gabbro (Axial Melt Lens- AML) is unconsolidated and separated from the overlying hydrothermal system by an thermal conductive boundary layer. $\delta^{34}S$ would be bounded by the current composition of the Upper Dikes. **(B)** The hydrothermal cells penetrate the now consolidated Lower Gabbro, while it is extensively intruded by new dikes. The thin Upper Gabbro is meanwhile emplaced and quickly consolidates above, being extensivelly modified by an isotopically enriched fluid. The diagrams on the right schematically show the isotope, sulfur and base metal loss profiles currently observed.

making further extrapolations to the actual relationship with the sulfur isotope compositions of VMS fluids.

Despite its unusual isotopic variations, the upper crustal section drilled in Hole GT3A has many of the ingredients of a deep reaction zone of a VMS hydrothermal system (Hannington, 2014). The degree of Cu mobilization here estimated (conservatilly based on Geotimes lavas, see section 5.3.1) is akin to that reported in diabases and epidosites of the Troodos ophiolite (Jowitt et al., 2012), although slightly lower for Zn. Integrated weighted averages for S and metals mobilised in the Hole GT3A Sequence (Table 4) show that 1 km^3 of crust can release ca. 2839 kt S, 107 kt Cu and 148 kt Zn. These values are within the range of the amount of metal released in the epidosite areas of Troodos (Jowitt et al., 2012). An average-sized VMS deposit in Oman hosted in axial Geotimes lavas has ~1 Mt. ore @ 2 % Cu = 20 kt, 0.5 % Zn = 5kt and is constituted by ~80 % of pyrite equating to 424 kt of sulfur (Cravinho et al., 2023; Gilgen et al., 2014), much less than the amount of metal estimated to be mobilised in Hole GT3A. A twofold area (2 km^3) would be necessary to produce a large 8 Mt. deposit like Mandoos (Cravinho et al., 2023). These results concur with observations by Nehlig et al. (1994), that hydrothermal leaching of metals and S do not necessarily require the formation of epidosites, which were not documented in Hole GT3A. The isotope shifts, and the most conservative estimates of metal and S leaching in Hole GT3A samples are far more extensive than reported in in-situ oceanic crust (Alt et al., 1996; Alt et al., 2010; Gillis, 1995; Gillis et al., 2001; Heft et al., 2008; Patten et al., 2016), reinforcing the view that ophiolitic crust experienced larger hydrothermal fluxes than in-situ Mid Ocean Ridges (Bickle and Teagle, 1992; Alt and Teagle, 2000).

6. Conclusions

The sheeted dike – gabbro transition sampled by Hole GT3A records wide variations in sulfur isotope compositions, with unusually high $\delta^{34}S$ values compared to in-situ or ophiolitic crust and an integrated composition of +5.8 ‰. The low sulfide-sulfur concentrations and heavy sulfur isotope signatures are consistent with abiogenic thermochemical sulfate reduction reactions during intense hydrothermal alteration under greenschist facies conditions. This produced a low-variance and relatively high-fS_2 assemblage of pyrite ± chalcopyrite ± bornite. The Lower Gabbro Sequence records minor sulfur additions and progressively lighter isotope signatures with depth which reflect decreasing availability of seawater derived sulfate in the hydrothermal fluid following the gabbro consolidation. The heaviest sulfur isotope compositions ($\delta^{34}S$ of +10 to +14 ‰) occur within ±10 m of the Upper Gabbro and can be explained by a focalized fluid that experienced isotope enrichment relative to seawater due to closed-system reservoir effects. The overlying Upper Sheeted Dike Sequence records $\delta^{34}S$ values closer to MORB values (<+5.1 ‰) due to magmatic sulfur leaching without associated hydrothermal sulfide deposition. This suggests the influence of a fluid buffered by magmatic S isotopic compositions, closer to the signatures of Oman VMS deposits. Rare negative $\delta^{34}S$ values resulted from late addition of small amounts of biogenic sulfur, likely during post-axial stages. Hole GT3A has all the features of a deep hydrothermal reaction zone with incorporation of up to ~80 % seawater derived sulfate and extensive S and Cu losses that were either re-precipitated at higher crustal levels or vented to the seafloor. The amount of metal released in a 1 km^3 crustal section like Hole GT3A represents ~3-fold the typical metal endowment of VMS deposits hosted in the axial lavas of Oman.

The mid to lower crustal section sampled by Holes GT2A and GT1A mostly preserves MORB sulfur isotope signatures and highly variable sulfur contents. Away from fault zones, a silicate microvein network enabled sulfide and metal remobilization of magmatic sulfide assemblages along with formation of millerite + siegenite-polydimite$_{ss}$ + pyrite. These reactions imply small additions of sulfur, expressed by progressive isotopic enrichment in metasomatic or hydrothermal sulfides relative to magmatic or remobilized sulfides. The mid-lower crustal section experienced redistribution of magmatic sulfur mixed with very small inputs of seawater-derived sulfur (< 10 %), under very low fluid/rock ratios, moderate sulfur fugacities that essentially preserved base metal abundances in secondary sulfides.

Strongly altered (sub-greenschist facies) domains related with the many faulted intervals in Holes GT1A and GT2A, record near-complete leaching of magmatic sulfides without the deposition of secondary sulfides. The extensive sulfur plus Cu mobilization and occurrence of sulfate with a Cretaceous seawater sulfate isotope composition attest to open system behavior of these structures, which are the expression of crustal scale channeled hydrothermal fluid flow and preserve a previously unaccounted sulfur budget introduced in the deep crust.

Supplementary data to this article can be found online at https://doi.org/10.1016/j.lithos.2024.107913.

CRediT authorship contribution statement

Ana P. Jesus: Writing – original draft, Visualization, Validation, Supervision, Resources, Project administration, Methodology, Investigation, Funding acquisition, Formal analysis, Data curation, Conceptualization. **Harald Strauss:** Writing – review & editing, Validation, Supervision, Resources, Methodology, Investigation, Funding acquisition, Formal analysis, Data curation. **Mário A. Gonçalves:** Writing – review & editing, Supervision, Formal analysis, Conceptualization. **Michelle Harris:** Writing – review & editing, Validation, Resources, Conceptualization. **Diogo Silva:** Investigation, Formal analysis, Data curation. **Martin J. Whitehouse:** Writing – review & editing, Methodology, Formal analysis, Data curation. **Damon A.H. Teagle:** Writing – review & editing, Validation, Supervision, Investigation.

Declaration of competing interest

The authors declare that they have no known competing financial interests or personal relationships that could have appeared to influence the work reported in this paper.

Acknowledgments

This work utilized samples from the Oman Drilling (OmanDP) that has been possible through co-mingled funds from the International Continental Scientific Drilling Project (ICDP; Kelemen, Matter, Teagle Lead PIs), the Sloan Foundation– Deep Carbon Observatory (Grant 2014-3-01, Kelemen PI), the National Science Foundation (NSF-EAR-1516300, Kelemen lead PI), NASA– Astrobiology Institute (NNA15BB02A, Templeton PI), the German Research Foundation (DFG: KO 1723/21-1, Koepke PI), the Japanese Society for the Promotion of Science (JSPS no:16H06347, Michibayashi PI; and KAKENHI 16H02742, Takazawa PI), the European Research Council (Adv: no.669972; Jamveit PI), the Swiss National Science Foundation (SNF:20FI21_163073, Früh-Green PI), JAMSTEC, the TAMU-JR Science Operator, and contributions from the Sultanate of Oman Ministry of Regional Municipalities and Water Resources, the Oman Public Authority of Mining, Sultan Qaboos University, CNRS-Univ. Montpellier, Columbia University of New York, and the University of Southampton. The NordSIMS facility in Stockholm operates as Swedish Research Council infrastructure (grant 2017-00256); this is NordSIMS publication ##781.

AJ received funding from WWU Fellowships for International Visiting Scholars, European Union's Horizon 2020 research and innovation program under the Marie Sklodowska-Curie grant agreement No 894599 and Instituto Dom Luiz FCT- I.P./MCTES through national funds (PIDDAC) – UIDB/50019/2020 (https://doi.org/10.54499/UIDB/50019/2020), UIDP/50019/2020 (https://doi.org/10.54499/UIDP/50019/2020) and LA/P/0068/2020 (https://doi.org/10.54499/LA/P/0068/2020). DT and MH were in part funded by NERC grant NE/

W007517/1. We are grateful to Dr. Esther Schwarzenbach for assisiting with modelling of sulfur geochemistry processes and to Dr Tom Belgrano for lively discussions on the geochemistry of the Oman lavas. Dr. Clifford Patten, Dr. Ville Virtannen, Manuel Dias and André Cravinho are warmly acknowledged for their support in modelling and software loggistics. Thoughtful comments and suggestions by Dr Barbara Kleine-Marshall and editorial handling of Dr Jeff Alt are sincerely appreciated.

References

Abily, B., Ceuleneer, G., Launeau, P., 2011. Synmagmatic normal faulting in the lower oceanic crust: Evidence from the Oman ophiolite. Geology 39, 391–394.

Alabaster, T., Pearce, J.A., Malpas, J., 1982. The Volcanic Stratigraphy and Petrogenesis of the Oman Ophiolite Complex. Contrib. Mineral. Petrol. 81, 168–183.

Alford, S.E., Alt, J.C., Shanks III, W.C., 2011. Sulfur geochemistry and microbial sulfate reduction during low-temperature alteration of uplifted lower oceanic crust: Insights from ODP Hole 735B. Chem. Geol. 286, 185–195.

Alt, J.C., 1994. A sulfur isotopic profile through the Troodos ophiolite, Cyprus: primary composition and the effects of seawater hydrothermal alteration. Geochim. Cosmochim. Acta 58, 1825–1840.

Alt, J.C., 1995. Subseafloor processes in mid-ocean ridge hydrothermal systems. Geophys. Monogr.-American Geophys. Union 91, 85–114.

Alt, J.C., Anderson, T.F., 1991. Mineralogy and isotopic composition of sulfur in layer 3 gabbros from the Indian Ocean, Hole 735B. Proc. Ocean Drill. Program Sci. Results 113–125.

Alt, J.C., Shanks, W.C., 2011. Microbial sulfate reduction and the sulfur budget for a complete section of altered oceanic basalts, IODP Hole 1256D (eastern Pacific). Earth Planet. Sci. Lett. 310, 73–83.

Alt, J.C., Teagle, D.A.H., 2000. Hydrothermal alteration and fluid fluxes in ophiolites and oceanic crust. In: Dilek, Y., Moores, E.M., Elthon, D., Nicolas, A. (Eds.), Ophiolites and Oceanic Crust: New Insights from Field Studies and the Ocean Drilling Program, 349. Geological Society of America, Sepcial Paper, pp. 273–282.

Alt, J.C., Anderson, T.F., Bonnell, L., 1989. The geochemistry of sulfur in a 1.3 km section of hydrothermally altered oceanic crust, DSDP Hole 504B. Geochim. Cosmochim. Acta 53, 1011–1023.

Alt, J.C., Zuleger, E., Erzinger, J., 1995. Mineralogy and stable isotopic compositions of the hydrothermally altered lower sheeted dike complex, Hole 504B, Leg 140. In: Proceedings of the Ocean Drilling Program, Scientific Results. Citeseer, pp. 155–166.

Alt, J.C., Laverne, C., Vanko, D.A., Tartarotti, P., Teagle, D.A., Bach, W., Zuleger, E., Erzinger, J., Honnorez, J., Pezard, P.A., 1996. Hydrothermal alteration of a section of upper oceanic crust in the Eastern Equatorial Pacific: a synthesis of results from site 504 (DSDP LEGS 69, 70, and 83, and ODP LEGS 111, 137,140, and 148). In: Proceedings of the Ocean Drilling Program, Scientific Results, pp. 417–434.

Alt, J.C., Shanks, W.C., Bach, W., Paulick, H., Garrido, C.J., Beaudoin, G., 2007. Hydrothermal alteration and microbial sulfate reduction in peridotite and gabbro exposed by detachment faulting at the Mid-Atlantic Ridge, 15° 20′ N (ODP Leg 209): A sulfur and oxygen isotope study. Geochem. Geophys. Geosyst. 8.

Alt, J.C., Laverne, C., Coggon, R.M., Teagle, D.A., Banerjee, N.R., Morgan, S., Smith-Duque, C.E., Harris, M., Galli, L., 2010. Subsurface structure of a submarine hydrothermal system in ocean crust formed at the East Pacific Rise, ODP/IODP Site 1256. Geochem. Geophys. Geosyst. 11.

Anonymous, 1972. Penrose field conference on ophiolites. Geotimes 17, 24–25.

Bach, W., Edwards, K.J., 2003. Iron and sulfide oxidation within the basaltic ocean crust: implications for chemolithoautotrophic microbial biomass production. Geochim. Cosmochim. Acta 67, 3871–3887.

Barker, A.K., Coogan, L.A., Gillis, K.M., 2010. Insights into the behaviour of sulphur in mid-ocean ridge axial hydrothermal systems from the composition of the sheeted dyke complex at Pito Deep. Chem. Geol. 275, 105–115.

Belgrano, T.M., Diamond, L.W., Vogt, Y., Biedermann, A.R., Gilgen, S., Al-Tobi, K., 2019. A revised map of volcanic units in the Oman ophiolite: insights into the architecture of an oceanic proto-arc volcanic sequence. Solid Earth 10, 1181–1217.

Benoit, M., Polvé, M., Ceuleneer, G., 1996. Trace element and isotopic characterization of mafic cumulates in a fossil mantle diapir (Oman ophiolite). Chem. Geol. 134, 199–214.

Bickle, M.J., Teagle, D.A., 1992. Strontium alteration in the Troodos ophiolite: implications for fluid fluxes and geochemical transport in mid-ocean ridge hydrothermal systems. Earth and Planetary Science Letters 113 (1–2), 219–237.

Bosch, D., Jamais, M., Boudier, F., Nicolas, A., Dautria, J.-M., Agrinier, P., 2004. Deep and high-temperature hydrothermal circulation in the Oman ophiolite—petrological and isotopic evidence. J. Petrol. 45, 1181–1208.

Cabral, R.A., Jackson, M.G., Rose-Koga, E.F., Koga, K.T., Whitehouse, M.J., Antonelli, M. A., Farquhar, J., Day, J., Hauri, E.H., 2013. Anomalous sulphur isotopes in plume lavas reveal deep mantle storage of Archaean crust. Nature 496, 490–493.

Canfield, D., 2001. Biogeochemistry of sulfur isotopes. Rev. Mineral. Geochem. 43, 607–636.

Canfield, D.E., 2004. The evolution of the Earth surface sulfur reservoir. Am. J. Sci. 304, 839–861.

Canfield, D.E., Raiswell, R., Westrich, J.T., Reaves, C.M., Berner, R.A., 1986. The use of chromium reduction in the analysis of reduced inorganic sulfur in sediments and shales. Chem. Geol. 54, 149–155.

Coogan, L.A., Mitchell, N.C., O'Hara, M.J., 2003. Roof assimilation at fast spreading ridges: An investigation combining geophysical, geochemical, and field evidence. J. Geophys. Res. Solid Earth 108. ECV 2-1-ECV 2-14.

Coogan, L., Howard, K., Gillis, K., Bickle, M., Chapman, H., Boyce, A., Jenkin, G., Wilson, R., 2006. Chemical and thermal constraints on focussed fluid flow in the lower oceanic crust. Am. J. Sci. 306, 389–427.

Cravinho, A., Jesus, A.P., Moreira, B., Mateus, A., Pracejus, B., Figueiras, J., Benoit, M., Bauer, W., Rocha, F., 2023. Contrasting Features and Volcanostratigraphy of the Mafic-Hosted Mandoos and Shinas Volcanogenic Massive Sulfide Deposits, Samail Ophiolite, Oman. Econ. Geol. 118 (5), 1085–1124.

Crowe, D., Vaughan, R., 1996. Characterization and use of isotopically homogeneous standards for in situ laser microprobe analysis of 34S/32 S ratios. Am. Mineral. 81, 187–193.

Delacour, A., Früh-Green, G.L., Bernasconi, S.M., 2008a. Sulfur mineralogy and geochemistry of serpentinites and gabbros of the Atlantis Massif (IODP Site U1309). Geochim. Cosmochim. Acta 72, 5111–5127.

Delacour, A., Früh-Green, G.L., Bernasconi, S.M., Kelley, D.S., 2008b. Sulfur in peridotites and gabbros at Lost City (30°N, MAR): Implications for hydrothermal alteration and microbial activity during serpentinization. Geochim. Cosmochim. Acta 72, 5090–5110.

Engelhardt, A., Koepke, J., Zhang, C., Garbe-Schönberg, D., Jesus, A.P., 2022. ICDP Oman Drilling Project: varitextured gabbros from the dike–gabbro transition within drill core GT3A. Eur. J. Mineral. 34, 603–626.

Farquhar, J., Jackson, T.L., Thiemens, M.H., 2000. A 33S enrichment in ureilite meteorites: evidence for a nebular sulfur component. Geochim. Cosmochim. Acta 64, 1819–1825.

Fleet, M.E., 2006. Phase equilibria at high temperatures. Rev. Mineral. Geochem. 61, 365–419.

France, L., Lombard, M., Nicollet, C., Berthod, C., Debret, B., Koepke, J., Ildefonse, B., Toussaint, A., 2021. Quantifying the axial magma lens dynamics at the roof of oceanic magma reservoirs (dike/gabbro transition): Oman Drilling Project GT3 site survey. J. Geophys. Res. Solid Earth 126 (5) e2020JB021496.

Fry, B., Ruf, W., Gest, H., Hayes, J.M., 1988. Sulfur isotope effects associated with oxidation of sulfide by O2 in aqueous solution. Chem. Geol.: Isotope Geosci. Sect. 73, 205–210.

Gale, A., Dalton, C.A., Langmuir, C.H., Su, Y., Schilling, J.G., 2013. The mean composition of ocean ridge basalts. Geochem. Geophys. Geosyst. 14, 489–518.

Gilgen, S.A., Diamond, L.W., Mercolli, I., Al-Tobi, K., Maidment, D.W., Close, R., Al-Towaya, A., 2014. Volcanostratigraphic Controls on the Occurrence of Massive Sulfide Deposits in the Semail Ophiolite, Oman. Econ. Geol. 109, 1585–1610.

Gilgen, S.A., Diamond, L.W., Mercolli, I., 2016. Sub-seafloor epidosite alteration: Timing, depth and stratigraphic distribution in the Semail ophiolite, Oman. Lithos 260, 191–210.

Gillis, K.M., 1995. Controls on hydrothermal alteration in a section of fast-spreading oceanic crust. Earth Planet. Sci. Lett. 134, 473–489.

Gillis, K.M., 2008. The roof of an axial magma chamber: A hornfelsic heat exchanger. Geology 36, 299–302.

Gillis, K.M., Muehlenbachs, K., Stewart, M., Gleeson, T., Karson, J., 2001. Fluid flow patterns in fast spreading East Pacific Rise crust exposed at Hess Deep. J. Geophys. Res. Solid Earth 106, 26311–26329.

Godard, M., Bosch, D., Einaudi, F., 2006. A MORB source for low-Ti magmatism in the Semail ophiolite. Chem. Geol. 234, 58–78.

Goodenough, K.M., Thomas, R.J., Styles, M.T., Schofield, D.I., MacLeod, C.J., 2014. Records of ocean growth and destruction in the Oman–UAE ophiolite. Elements 10, 109–114.

Hannington, M., 2014. Volcanogenic massive sulphide deposits. In: Holland, H.D., Turekian, K.K. (Eds.), Treatise on geochemistry, 2nd edition. Elsevier Ltd.

Harper, G.D., Bowman, J.R., Kuhns, R., 1988. A field, chemical, and stable isotope study of subseafloor metamorphism of the Josephine ophiolite, California-Oregon. J. Geophys. Res. Solid Earth 93, 4625–4656.

Harris, M., Coggon, R.M., Smith-Duque, C.E., Cooper, M.J., Milton, J.A., Teagle, D.A.H., 2015. Channelling of hydrothermal fluids during the accretion and evolution of the upper oceanic crust: Sr isotope evidence from ODP Hole 1256D. Earth Planet. Sci. Lett. 416, 56–66.

Heft, K.L., Gillis, K.M., Pollock, M.A., Karson, J.A., Klein, E.M., 2008. Role of upwelling hydrothermal fluids in the development of alteration patterns at fast spreading ridges: Evidence from the sheeted dike complex at Pito Deep. Geochem. Geophys. Geosyst. 9.

Jesus, A.P., Strauss, H., Benoit, M., Goncalves, M., Santos, A., 2022. Strontium and multiple sulfur isotopic constraints on Volcanogenic Massive Sulfide (VMS). In: deposits in the Oman ophiolite, 2022 Goldschmidt Conference. GOLDSCHMIDT.

Johnston, D.T., Gill, B.C., Masterson, A., Beirne, E., Casciotti, K.L., Knapp, A.N., Berelson, W., 2014. Placing an upper limit on cryptic marine sulphur cycling. Nature 513, 530–533.

Jowitt, S.M., Jenkin, G.R., Coogan, L.A., Naden, J., 2012. Quantifying the release of base metals from source rocks for volcanogenic massive sulfide deposits: Effects of protolith composition and alteration mineralogy. J. Geochem. Explor. 118, 47–59.

Kampschulte, A., Strauss, H., 2004. The sulfur isotopic evolution of Phanerozoic seawater based on the analysis of structurally substituted sulfate in carbonates. Chem. Geol. 204, 255–286.

Kelemen, P.B., Koga, K., Shimizu, N., 1997. Geochemistry of gabbro sills in the crust-mantle transition zone of the Oman ophiolite: implications for the origin of the oceanic lower crust. Earth Planet. Sci. Lett. 146, 475–488.

Kelemen, P., Matter, J., Teagle, D.A.H., Coggon, J.A., Team, O.D.P.S, 2020. Proceedings of the Oman Drilling Project: College Station, TX (International Ocean Discovery Program).

Kleine, B.I., Stefánsson, A., Zierenberg, R.A., Jeon, H., Whitehouse, M.J., Jónasson, K., Fridleifsson, G.Ó., Weisenberger, T.B., 2022. Sulfate (re-) cycling in the oceanic crust: Effects of seawater-rock interaction, sulfur reduction and temperature on the

abundance and isotope composition of anhydrite. Geochim. Cosmochim. Acta 317, 65–90.
Koepke, J., Schoenborn, S., Oelze, M., Wittmann, H., Feig, S., Hellebrand, E., Boudier, F., Schoenberg, R., 2009. Petrogenesis of crustal wehrlites in the Oman ophiolite: Experiments and natural rocks. Geochem. Geophys. Geosyst. 10, n/a-n/a.
Labidi, J., Cartigny, P., Birck, J.L., Assayag, N., Bourrand, J.J., 2012. Determination of multiple sulfur isotopes in glasses: A reappraisal of the MORB δ34S. Chem. Geol. 334, 189–198.
Labidi, J., Cartigny, P., Hamelin, C., Moreira, M., Dosso, L., 2014. Sulfur isotope budget (32S, 33S, 34S and 36S) in Pacific–Antarctic ridge basalts: A record of mantle source heterogeneity and hydrothermal sulfide assimilation. Geochim. Cosmochim. Acta 133, 47–67.
LaFlamme, C., Martin, L., Jeon, H., Reddy, S.M., Selvaraja, V., Caruso, S., Bui, T.H., Roberts, M.P., Voute, F., Hagemann, S., 2016. In situ multiple sulfur isotope analysis by SIMS of pyrite, chalcopyrite, pyrrhotite, and pentlandite to refine magmatic ore genetic models. Chem. Geol. 444, 1–15.
Lecuyer, C., Reynard, B., 1996. High-temperature alteration of oceanic gabbros by seawater (Hess Deep, Ocean Drilling Program Leg 147): Evidence from oxygen isotopes and elemental fluxes. J. Geophys. Res. Solid Earth 101, 15883–15897.
Li, C., Ripley, E.M., 2009. Sulfur contents at sulfide-liquid or anhydrite saturation in silicate melts: empirical equations and example applications. Econ. Geol. 104, 405–412.
Li, R., Xia, X., Yang, S., Chen, H., Yang, Q., 2019. Off-mount calibration and one new potential pyrrhotite reference material for sulfur isotope measurement by secondary ion mass spectrometry. Geostand. Geoanal. Res. 43, 177–187.
Lippard, S.J., 1986. The ophiolite of northern Oman. Geol. Soc. Lond. Mem. 11, 178.
Liseroudi, M.H., Ardakani, O.H., Pedersen, P.K., Stern, R.A., Wood, J.M., Sanei, H., 2021. Microbial and thermochemical controlled sulfur cycle in the Early Triassic sediments of the Western Canadian Sedimentary Basin. J. Geol. Soc. 178 jgs2020-2175.
Liu, Y., Samaha, N.-T., Baker, D.R., 2007. Sulfur concentration at sulfide saturation (SCSS) in magmatic silicate melts. Geochim. Cosmochim. Acta 71, 1783–1799.
MacLeod, C.J., Yaouancq, G., 2000. A fossil melt lens in the Oman ophiolite: Implications for magma chamber processes at fast spreading ridges. Earth Planet. Sci. Lett. 176, 357–373.
Manning, C.E., MacLeod, C.J., Weston, P.E., 2000. Lower-crustal cracking front at fast-spreading ridges: Evidence from the East Pacific Rise and the Oman ophiolite. Spe. Paper.-Geol. Soc. America 261–272.
Masterson, A., Wing, B.A., Paytan, A., Farquhar, J., Johnston, D.T., 2016. The minor sulfur isotope composition of Cretaceous and Cenozoic seawater sulfate. Paleoceanography 31, 779–788.
Mathez, E., 1976. Sulfide relations in hole 418a flows and sulfur contents of glasses. In: Initial Reports of the Deep Sea Drilling Project: A Project Planned by and Carried Out with the Advice of the Joint Oceanographic Institutions for Deep Earth Sampling, 51, p. 1069.
McCollom, T.M., Shock, E.L., 1998. Fluid-rock interactions in the lower oceanic crust: Thermodynamic models of hydrothermal alteration. J. Geophys. Res. Solid Earth 103, 547–575.
Nehlig, P., Juteau, T., Bendel, V., Cotten, J., 1994. The root zones of oceanic hydrothermal systems: Constraints from the Samail ophiolite (Oman). J. Geophys. Res. Solid Earth 1978–2012 (99), 4703–4713.
Nicolas, A., Boudier, F., Ildefonse, B., Ball, E., 2000. Accretion of Oman and United Arab Emirates ophiolite–Discussion of a new structural map. Mar. Geophys. Res. 21, 147–180.
Oeser, M., Strauss, H., Wolff, P.E., Koepke, J., Peters, M., Garbe-Schönberg, D., Dietrich, M., 2012. A profile of multiple sulfur isotopes through the Oman ophiolite. Chem. Geol. 312, 27–46.
Ohmoto, H., Lasaga, A.C., 1982. Kinetics of reactions between aqueous sulfates and sulfides in hydrothermal systems. Geochim. Cosmochim. Acta 46, 1727–1745.
Ohmoto, H., Rye, R., Barnes, H., 1979. Geochemistry of Hydrothermal Ore Deposits.
Ono, S., Shanks III, W.C., Rouxel, O.J., Rumble, D., 2007. S-33 constraints on the seawater sulfate contribution in modern seafloor hydrothermal vent sulfides. Geochim. Cosmochim. Acta 71, 1170–1182.
Pallister, J.S., Hopson, C.A., 1981. Samail Ophiolite Plutonic Suite - Field Relations, Phase Variation, Cryptic Variation and Layering, and a Model of a Spreading Ridge Magma Chamber. J. Geophys. Res. 86, 2593–2644.
Patten, C.G., Pitcairn, I.K., Teagle, D.A., Harris, M., 2016. Mobility of Au and related elements during the hydrothermal alteration of the oceanic crust: implications for the sources of metals in VMS deposits. Mineral. Deposita 51, 179–200.
Paytan, A., Kastner, M., Campbell, D., Thiemens, M.H., 2004. Seawater sulfur isotope fluctuations in the Cretaceous. Science 304, 1663–1665.
Peters, M., Strauss, H., Farquhar, J., Ockert, C., Eickmann, B., Jost, C.L., 2010. Sulfur cycling at the Mid-Atlantic Ridge: A multiple sulfur isotope approach. Chem. Geol. 269, 180–196.
Peters, M., Strauss, H., Petersen, S., Kummer, N.-A., Thomazo, C., 2011. Hydrothermalism in the Tyrrhenian Sea: Inorganic and microbial sulfur cycling as revealed by geochemical and multiple sulfur isotope data. Chem. Geol. 280, 217–231.
Plank, T., Manning, C.E., 2019. Subducting carbon. Nature 574, 343–352.
Puchelt, H., Prichard, H., Berner, Z., Maynard, J., 1996. Sulfide mineralogy, sulfur content, and sulfur isotope composition of mafic and ultramafic rocks from Leg 147. In: Proceedings-Ocean Drilling Program Scientific Results. National Science foundation, pp. 91–102.
Rice, C.A., Tuttle, M.L., Reynolds, R.L., 1993. The analysis of forms of sulfur in ancient sediments and sedimentary rocks: comments and cautions. Chem. Geol. 107, 83–95.
Richardson, C.J., Cann, J.R., Richards, H.G., Cowan, J.G., 1987. Metal-depleted root zones of the Troodos ore-forming hydrothermal systems, Cyprus. Earth Planet. Sci. Lett. 84, 243–253.
Richter, L., Diamond, L.W., 2022. Characterization of hydrothermal fluids that alter the upper oceanic crust to spilite and epidosite: Fluid inclusion evidence from the Semail (Oman) and Troodos (Cyprus) ophiolites. Geochim. Cosmochim. Acta 319, 220–253.
Rioux, M., Garber, J.M., Searle, M., Kelemen, P., Miyashita, S., Adachi, Y., Bowring, S., 2021. High-precision U-Pb zircon dating of late magmatism in the Samail ophiolite: A record of subduction initiation. J. Geophys. Res. Solid Earth 126, e2020JB020758.
Sakai, H., Des Marais, D., Ueda, A., Moore, J., 1984. Concentrations and isotope ratios of carbon, nitrogen and sulfur in ocean-floor basalts. Geochim. Cosmochim. Acta 48, 2433–2441.
Salters, V.J., Stracke, A., 2004. Composition of the depleted mantle. Geochem. Geophys. Geosyst. 5.
Schwarzenbach, E.M., Gill, B.C., Johnston, D.T., 2018. Unraveling multiple phases of sulfur cycling during the alteration of ancient ultramafic oceanic lithosphere. Geochim. Cosmochim. Acta 223, 279–299.
Seyfried Jr., W., Bischoff, J.L., 1981. Experimental seawater-basalt interaction at 300 C, 500 bars, chemical exchange, secondary mineral formation and implications for the transport of heavy metals. Geochim. Cosmochim. Acta 45, 135–147.
Seyfried Jr., W.E., Ding, K., Berndt, M.E., Chen, X., 1997. Experimental and Theoretical Controls on the Composition of Mid-Ocean Ridge Hydrothermal Fluids, Volcanic Associated Massive Sulfide Deposits: Processes and Examples in Modern and Ancient Settings. Society of Economic Geologists, p. 0.
Shanks, W.C., 2001. Stable isotopes in seafloor hydrothermal systems: vent fluids, hydrothermal deposits, hydrothermal alteration, and microbial processes. Rev. Mineral. Geochem. 43, 469–525.
Shanks, W.C., Bischoff, J.L., Rosenbauer, R.J., 1981. Seawater sulfate reduction and sulfur isotope fractionation in basaltic systems: Interaction of seawater with fayalite and magnetite at 200–350°C. Geochim. Cosmochim. Acta 45, 1977–1995.
Sleep, N.H., 1991. Hydrothermal circulation, anhydrite precipitation, and thermal structure at ridge axes. J. Geophys. Res. Solid Earth 96, 2375–2387.
Staudigel, H., 2014. Chemical fluxes from hydrothermal alteration of the oceanic crust.
Taylor, B.E., Wheeler, M.C., Nordstrom, D.K., 1984. Stable isotope geochemistry of acid mine drainage: Experimental oxidation of pyrite. Geochim. Cosmochim. Acta 48, 2669–2678.
Teagle, D.A., Alt, J.C., Halliday, A.N., 1998. Tracing the chemical evolution of fluids during hydrothermal recharge: Constraints from anhydrite recovered in ODP Hole 504B. Earth Planet. Sci. Lett. 155, 167–182.
Teagle, D.A., Ildefonse, B., Blum, P., 2010. Integrated Ocean Drilling Program Expedition 335 Scientific Prospectus Superfast Spreading Rate Crust 4.
Teagle, D., Cooper, M., Harris, M., Crispini, L., Kelemen, P., 2019. Tethyan anhydrite preserved in the lower crust of the Samail ophiolite: Evidence from Oman Drilling Project Holes GT1A and 2A. Geophys. Res. Abstr.
Timofeeff, M.N., Lowenstein, T.K., Da Silva, M.A.M., Harris, N.B., 2006. Secular variation in the major-ion chemistry of seawater: Evidence from fluid inclusions in Cretaceous halites. Geochim. Cosmochim. Acta 70, 1977–1994.
White, W., Klein, E., 2014. 4.13-Composition of the oceanic crust. Treatise on. Geochemistry 457–496 (second edition).
Whitehouse, M.J., 2013. Multiple sulfur isotope determination by SIMS: Evaluation of reference sulfides for Δ33S with observations and a case study on the determination of Δ36S. Geostand. Geoanal. Res. 37, 19–33.
Whitehouse, M.J., Kamber, B.S., Fedo, C.M., Lepland, A., 2005. Integrated Pb- and S-isotope investigation of sulphide minerals from the early Archaean of southwest Greenland. Chem. Geol. 222, 112–131.
Wilson, D.S., Teagle, D.A., Alt, J.C., Banerjee, N.R., Umino, S., Miyashita, S., Acton, G.D., Anma, R., Barr, S.R., Belghoul, A., 2006. Drilling to gabbro in intact ocean crust. Science 312, 1016–1020.
Woodruff, L.G., Shanks III, W.C., 1988. Sulfur isotope study of chimney minerals and vent fluids from 21 N, East Pacific Rise: hydrothermal sulfur sources and disequilibrium sulfate reduction. J. Geophys. Res. Solid Earth 93, 4562–4572.
Zhang, C., Koepke, J., Wolff, P.E., Horn, I., Garbe-Schönberg, D., Berndt, J., 2021. Multi-Stage Hydrothermal Veins in Layered Gabbro of the Oman Ophiolite: Implications for Focused Fluid Circulation in the Lower Oceanic Crust. J. Geophys. Res. Solid Earth 126, e2021JB022349.
Zihlmann, B., Müller, S., Coggon, R.M., Koepke, J., Garbe-Schönberg, D., Teagle, D.A., 2018. Hydrothermal fault zones in the lower oceanic crust: An example from Wadi Gideah, Samail ophiolite, Oman. Lithos 323, 103–124.